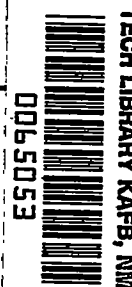


8627

NACA TN 2203



NATIONAL ADVISORY COMMITTEE FOR AERONAUTICS

TECHNICAL NOTE 2203

BOUNDARY-LAYER MEASUREMENTS IN 3.84- BY 10-INCH
SUPERSONIC CHANNEL

By Paul F. Brinich

Lewis Flight Propulsion Laboratory
Cleveland, Ohio



Washington

October 1950

AF 50
TECHNICAL NOTE 2203
OCT 1950

319.95/41



NATIONAL ADVISORY COMMITTEE FOR AERONAUTICS

TECHNICAL NOTE 2203

BOUNDARY-LAYER MEASUREMENTS IN 3.84- BY 10-INCH

SUPERSONIC CHANNEL

By Paul F. Brinich

SUMMARY

Boundary-layer measurements were made in the transonic and supersonic regions of a channel having maximum cross-sectional dimensions 3.84 by 10 inches and designed by potential-flow methods for a uniform Mach number of 2.08 in the test section. At inlet pressures from 37 to 13 inches of mercury absolute, turbulent boundary layers were observed throughout the channel; at an inlet pressure of 5 inches, laminar boundary layers were observed near the channel entrance with turbulent layers downstream.

A comparison of the experimental and theoretically computed boundary layers at the high inlet pressures showed good agreement when empirical friction coefficients were evaluated from Reynolds numbers based on the kinematic viscosity of the air at the wall. Despite this agreement between experiment and theory, local differences in rates of boundary-layer growth still existed that are attributed to secondary flows in the boundary layer.

At low inlet pressures, substantial increases in the boundary-layer rates of growth with an uneven development of the boundary layer along the bottom wall of the channel were observed.

Experimental and empirical skin-friction coefficients were in poor agreement at all inlet pressures. Secondary flows in the boundary layer caused by static-pressure gradients transverse to the stream direction are believed to be the reasons for the poor agreement.

INTRODUCTION

A knowledge of viscous effects in transonic and supersonic flows has become increasingly important because of the demand for improved accuracy in the prediction of high-speed flight phenomena. In particular, viscous effects on the walls of supersonic channels

may profoundly affect the uniformity of the flow in the test stream, thereby imposing limitations on the usefulness of such channels for investigating the flow on models.

The potential flow in a supersonic channel may be readily determined by the methods of references 1 and 2. In reference 3, a method is proposed for predicting the turbulent boundary-layer development for two-dimensional flows with pressure gradient. In this method, the velocity profile is approximated by a power profile and the particular power profile and the value of skin-friction coefficient are obtained from empirical laws for turbulent boundary layers. Because these laws were formulated from results obtained at low speeds (reference 4), the validity of their extension to boundary layers in supersonic streams is not apparent.

The present study, which was conducted at the NACA Lewis laboratory, presents: (1) an evaluation of the method of reference 3 for predicting the boundary-layer development along the contour walls and the side walls of a typical supersonic channel; and (2) an investigation of the validity of the power-profile parameter and the skin-friction coefficient assumed in the method. The actual flow in a two-dimensional supersonic channel, however, differs from the idealized flow assumed in the analysis in reference 3 because of corner effects and secondary flows; hence a precise check between experiment and theory should not be expected. An attempt was therefore made to account for the differences between experiment and theory in terms of secondary-flow phenomena and to evaluate these effects qualitatively in the channel investigated.

APPARATUS

A diagram of the 3.84- by 10-inch test channel used in this investigation with the adjacent surge chamber, diffuser, piping, valves, and screen and pertinent dimensions is shown in figure 1. The maximum pressure attainable at the inlet was 40 inches of mercury absolute and the minimum exhaust pressure was $1\frac{1}{2}$ inches of mercury absolute.

The supersonic nozzle was designed to give a potential-flow Mach number of 2.08 by the method of reference 1 with a throat of conservatively large radius and is shown to scale in figure 2. The bellmouth contraction, the contour of which is not shown in figure 2, consisted of smoothly faired surfaces generating an area contraction ratio of 12.

The entire channel from the bellmouth inlet to the subsonic diffuser was constructed of stainless steel machined and polished to a maximum surface irregularity of 10 microinches. Nozzle coordinates were accurate to ± 0.010 inch.

The locations at which the boundary-layer total-pressure surveys were made are also shown in figure 2. Static-pressure orifices 0.013 to 0.020 inch in diameter were placed at these locations and four thermocouples were embedded in the side wall near the surface at the positions indicated.

Both single-tube and rake probes were used for measuring the boundary-layer profiles. The single-tube-probe tips were made of stainless-steel tubing having a 0.020-inch outside diameter flattened to 0.006-inch outside thickness. The rake-probe tips varied from 0.015- to 0.050-inch diameter. Some of the 0.015-inch-diameter tips were flattened to 0.005-inch outside thickness, others to 0.010, and still others were left circular; the flattened tips were nearest the wall.

The length of the probes was determined by noting how far upstream the wall static pressure was disturbed when a dummy-probe support was introduced into the stream. The probe was then designed to place the tip considerably upstream of this point. The four probes used in this investigation are shown in figure 3. Probes a and b were 3 inches long, c was 4 inches, and d was variable from 6 to 12 inches. Probe d did not possess sufficient rigidity for great accuracy but the length was necessary for transonic and subsonic measurements.

PROCEDURE

Boundary-layer surveys were made in the positions indicated in figure 2 using probes a, b, and d on the side wall and probe c on the bottom wall. Probe d was used at $x \leq 5.3$ inches, probe b at $x \geq 9.3$ inches, and probe a at several positions to check the measurements of probe b, where x is the distance in inches downstream of the geometrical throat of the nozzle.

For each x location of the probe, the stagnation pressure was varied from 37 to 5 inches of mercury absolute for most of the runs, although some of the results presented range from 40 to 5 inches. The increments between the various inlet pressures investigated varied from 4 to 24 inches of mercury; the smaller increment was used in the pressure range at which appreciable

changes in the boundary-layer development took place. The inlet temperature and dew-point temperature at atmospheric pressure were selected as 130° and -20° F, respectively, to give condensation-free flow at all inlet pressures. Pressure data were taken only after the channel side-wall temperature reached equilibrium, as indicated by the embedded thermocouples.

The conventional equations for reducing pressure data to Mach number using subsonic and supersonic pitot tubes were used (reference 2, pp. 26 and 77).

EXPERIMENTAL ACCURACY

The maximum total variations of the stagnation conditions during a given boundary-layer survey or from one run to another from the conditions previously stated were:

Reservoir pressure, in. Hg	±0.05
Reservoir temperature, °F	±3
Dew point at atmospheric pressure, °F	±8

In evaluating the accuracy of the boundary-layer total-pressure measurements, three sources of possible error must be considered: (1) manometer error, (2) probe-positioning error, and (3) probe influence on the boundary layer.

As a conservative value, the maximum manometer error was estimated at a consistent ±0.1 inch of mercury for a given survey and had its greatest effect on the computed values of M , δ^* , and θ when applied to the static-pressure measurement. (The symbols used herein are defined in the appendix.) The chief probe-positioning error was in zeroing the probe against the channel wall and had a consistent maximum value of ±0.002 inch for probes a, b, and c and ±0.005 inch for probe d for a given survey. At inlet pressures of 37, 13, and 5 inches of mercury absolute and Mach number of 2.0, the maximum errors due to manometer and positioning errors are summarized in the following table:

Inlet pressure P_0 (in. Hg)	Error in M (percent)	Error in $\bar{\delta}$ (percent)	Error in δ^* (percent)	Error in θ (percent)
37	2.3	0.5	2.0	0.5
13	6.7	.5	2.6	1.4
5	17.3	.5	6.7	3.4

For stations upstream of the test section, where the static pressure increases, the percentage error in measuring Mach number should be less than the values shown in the preceding table for a given inlet pressure. The percentage error in δ^* and θ , however, should increase as the probe is moved upstream because the increased positioning error associated with reduced boundary-layer thicknesses will overbalance decreased errors in measuring Mach number.

Other errors, such as those resulting from the influence of the probe on the boundary layer, could not be checked quantitatively. The observation was made, however, that static pressures increased up to 2 percent as the probe tip approached the wall. This effect was present with probes of length 3 to 12 inches and could not be eliminated by lengthening the probe.

A comparison of boundary-layer-profile measurements using the single-tube probe (probe a) and the rake (probe b) showed excellent agreement in measured values of M_1 and δ . A random variation in the profile shape from one test to another obtained from both probes, however, produced a variation of 0 to 10 percent in the value of δ^* . The effective probe center was considered to be at the geometrical center of the probe tip.

The accuracy of the temperature measurements on the side wall was $\pm 2^\circ \text{F}$.

RESULTS AND DISCUSSION

Mach Number Distributions along Channel

A requisite for evaluating the experimental flow measurements of this investigation is that the theoretical potential-flow Mach number distribution throughout the channel be known. In order to obtain the theoretical Mach number distributions along the curved bottom-wall and the flat side-wall center lines in the supersonic part of the channel, the method of characteristics (reference 2) using the assumption of uniform parallel flow in the nozzle throat was employed. These distributions are indicated in figure 4.

Shown also in figure 4 are the experimental stream Mach number distributions for a range of inlet pressures P_0 of 5 to 40 inches of mercury absolute. The Mach number was computed by two methods: (1) from measured local total and static pressures, and (2) from measured inlet total and local static pressures. Mach

numbers in the test section computed by the first method decreased on the bottom wall (fig. 4(a)) as the inlet pressure was reduced and increased on the side wall (fig. 4(b)). Conversely, the Mach numbers computed from measured inlet total and local static pressures with no probes in the stream increased on both walls with decreasing pressures. No reason for this behavior is known.

Further comparisons of the Mach number at P_0 values of 13 and 5 inches of mercury (fig. 4) showed large irregularities in the distribution when Mach number was computed by the first method and smooth distributions when using the second. Part of the irregularity in using the first method was no doubt caused by decreased accuracy in the low-pressure results, but the greater portion of it is believed to be due to actual irregularities in the air flow, possibly weak shock waves. These irregularities in the flow did not affect the static pressure at the wall and hence are not indicated in the Mach number computed by assuming a constant stagnation pressure.

The Mach number distributions obtained from the inlet total and local static pressures were included in figure 4 for comparison only and were not used in the analysis of the results. The curves of theoretical potential flow, corrected for experimental boundary-layer development, will be discussed in the section "Boundary-Layer Development."

Another observation to be made from figure 4 is that the experimental Mach numbers obtained from local total and static pressure frequently exceed the potential-flow values at P_0 of 13 and 5 inches of mercury. Although the amounts that these Mach numbers exceed the potential-flow values are very close to the maximum experimental error, the consistency of these results and the appearance of the same results in independent, unpublished tests corroborate the present findings. Also, the values on the side wall are much higher than those on the bottom wall at these low pressures for a large part of the channel length.

Lastly, a comparison of the Mach number distributions for P_0 of 37 and 21 inches of mercury (fig. 4(b)) shows them to be practically the same, which means that no significant changes in the potential-flow distribution or boundary-layer development occurred in this pressure range.

Temperature Recovery and Prandtl Number

Experimental recovery factors η_r were computed from measured reservoir temperature T_0 , measured channel-wall surface temperature T_w , and computed stream temperature T_1 based on local experimental Mach number and were defined by

$$\eta_r = \frac{T_w - T_1}{T_0 - T_1}$$

These values of η_r were then compared with theoretical values for an insulated plate given by the one-third power of the Prandtl number Pr (reference 5), where the value of Pr was a function of the temperature at the wall (reference 6). The following table summarizes these results:

x (in.)	M_1	T_w (°F)	η_r	$Pr^{1/3}$
-1.3	0.88	118	0.852	0.888
18.3	1.76	102	.876	.889
36.3	2.04	98	.881	.890
54.3	2.01	98	.879	.890

At the first position, where the wall temperature was about 40° F above room temperature, the value of η_r was about 4 percent below $Pr^{1/3}$; whereas at the three remaining positions, for which the wall temperature was only about 20° F above room temperature, the value of η_r was less than $\frac{1}{2}$ percent below $Pr^{1/3}$. These results indicate that heat transfer through the walls is small and may probably be neglected in computing velocities in the boundary layer and other boundary-layer quantities.

The assumption of zero heat transfer made in reference 3 and used in the present analysis has been shown to be approximately correct, but a question still remains concerning the error introduced by considering the Prandtl number equal to 1 in the interpretation of the data. This problem is analyzed in detail in reference 7, where it was found that the use of $Pr = 1$ led to an error of 3 percent in the velocity near the wall surface, which rapidly diminished to 0 as the free stream ($M = 2.0$) was approached. As a result of these errors in velocity, subsequent errors of 0.1 percent were introduced in δ^* and θ . The errors introduced into the skin-friction measurements also were small. The simplifying

assumptions of zero heat transfer and a Prandtl number of 1 used in the following analysis therefore appear to be justified.

Boundary-Layer Development

Experimental boundary-layer development. - Nondimensional boundary-layer velocity profiles u/u_∞ against y/δ for the side wall in the transonic-flow region of the channel (nozzle throat) at various inlet pressures are plotted in figure 5. The boundary-layer thickness δ is defined as that distance in the y -direction (perpendicular to the wall) at which the velocity $u = 0.99 u_\infty$, where u_∞ is the asymptotic stream velocity. These profiles were measured throughout a range of free-stream Mach numbers from 0.57 to 1.68. The profiles at P_0 of 37 and 13 inches of mercury are typical turbulent profiles throughout; whereas those at P_0 of 5 inches are laminar for $x \leq 5.3$ inches and turbulent for $x \geq 9.3$ inches. Theoretical laminar profiles (reference 8) assuming no heat transfer are also presented for the lowest inlet pressure corresponding to the experimental Mach numbers at x of -6.7 and 5.3 inches. Because the theoretical laminar profiles were based on flat-plate theory, whereas the experimental layers appeared in a highly favorable pressure gradient, the disagreement between the two should not be surprising. The similarity of the slopes near the wall, however, identifies the experimental profiles as laminar.

Nondimensional velocity profiles of the boundary layer throughout the entire channel are presented in figure 6 at P_0 of 37 inches of mercury for both the bottom and side walls. Logarithmic coordinates were used to facilitate comparisons between the theoretical power-law profiles and the experimental points. The theoretical profiles are represented by the straight lines with the appropriate value of the power-profile parameter N , which defines the shape of the theoretical boundary-layer power profile given by

$$\frac{u}{u_\infty} = \left(\frac{y}{\delta} \right)^{1/N} \quad (2)$$

In comparing the experimental and theoretical profiles, it is seen that the best agreement is reached at the greater distances downstream, which correspond to the regions of near zero pressure gradient. The results shown in figure 6 will be further analyzed in a following discussion of the power-profile parameter.

The boundary-layer development in terms of the boundary-layer thickness δ , the displacement thickness δ^* , and the momentum

thickness δ for the bottom and side walls at inlet pressures from 37 to 5 inches of mercury absolute are presented in figure 7. Also included are curves faired near the experimental points that were used in evaluating skin-friction coefficients.

The boundary-layer developments for P_0 of 37 inches of mercury on the bottom and side walls are characterized by smooth distributions of $\bar{\delta}$, δ^* , and θ along the channel length. The development for P_0 of 21 inches of mercury along the side wall (not shown in fig. 7(b)) was nearly the same as that obtained for P_0 of 37 inches of mercury. Decreases in inlet pressure below 21 inches of mercury resulted in increases in the rate of boundary-layer growth in the turbulent regions and decreases in the laminar regions. In addition, the boundary-layer developments along the bottom wall and the Mach number distributions of figure 4(a) (computed from local total and static pressures) become highly irregular. These irregularities in the boundary-layer development are not caused primarily by the decreased accuracy of the low-pressure measurements, but rather reflect the actual irregularity of the boundary-layer thickness, the measurement of which does not strongly depend on the accuracy of the pressure measurements.

Another characteristic of the low inlet-pressure results is the apparent incompatibility of the Mach number distributions along the channel with the boundary-layer development. Boundary-layer displacement thicknesses are considerably greater for the low-pressure flow downstream in the channel and less in the throat region; yet substantial increases in Mach number were noticed as the inlet pressure was reduced. This anomaly was previously pointed out when it was shown that the experimental Mach number exceeded the theoretical potential-flow Mach number at low pressures. Comparison of the theoretical Mach number distribution, which has been corrected for the presence of the experimental displacement thickness, with the experimental Mach number distribution throughout the range of inlet pressures emphasizes this anomaly. Curves of theoretical Mach number corrected for δ^* are given in figure 4 for the bottom and side walls. In correcting the potential-flow Mach number it was assumed that transverse to the stream direction the boundary layer was of constant thickness and velocity distribution. The geometric channel-area ratios were then corrected for the displacement thickness and, with the assumption of one-dimensional flow, the corrected potential flow Mach numbers were obtained.

A comparison of the corrected potential flow and experimental Mach number distributions in figure 4 indicates better agreement

for the high-inlet-pressure range than for the low pressures. As P_0 is progressively reduced to 13 and 5 inches of mercury, increasing disagreement is noted, that is, the corrected potential-flow Mach number is generally less than the experimental. The boundary-layer displacement thickness is believed to vary in a direction transverse to the stream, thereby invalidating the one-dimensional area-ratio correction. The presence of such nonuniformity of the boundary layer is possible if secondary flows are present. The variation in the discrepancy between the experimental and corrected potential-flow Mach numbers in figure 4 as the inlet pressure is changed suggests a variation in the intensity of the secondary flows with Reynolds number.

Reynolds number and transition. - In reference 3, two definitions of Reynolds number were investigated in the determination of the turbulent skin-friction coefficient in a pressure gradient. One definition is based on the kinematic viscosity of the free stream v_1 and the other, on the kinematic viscosity of the air adjacent to the wall in the boundary layer v_w . They may be written as

$$Re_{\bar{x},1} = \frac{u_1 \bar{x}_1}{v_1} \quad (3a)$$

and

$$Re_{\bar{x},w} = \frac{u_1 \bar{x}_w}{v_w} \quad (3b)$$

The terms \bar{x}_1 and \bar{x}_w are the equivalent lengths of turbulent run on a flat plate necessary to produce a known boundary-layer momentum thickness. These lengths of run were computed assuming a flat-plate skin-friction coefficient dependent on Reynolds number based on stream and wall kinematic viscosities, respectively.

The preceding methods for evaluating Reynolds number are indirect and may be replaced by more convenient definitions when θ is known; such as

$$Re_{\theta,1} = \frac{u_1 \theta}{v_1} \quad (4a)$$

and

$$Re_{\theta,w} = \frac{u_1 \theta}{v_w} \quad (4b)$$

The applicability of these two definitions of Reynolds number will be investigated further in the discussion of the skin-friction coefficient.

Laminar boundary layers were observed at P_0 of 5 inches of mercury for values of $x \leq 5.3$ inches on the side wall. At x of 9.3 inches (the next position investigated) and at greater distances downstream, turbulent layers were found. Reynolds numbers $Re_{\theta,1}$ and $Re_{\theta,w}$ and those based on δ^* , $Re_{\delta^*,1}$ and $Re_{\delta^*,w}$ at x of 5.3 and 9.3 inches are listed with values given by Goldstein (reference 9) for the commencement of transition in the following table:

	Distance from throat, x (in.)		Transition (Goldstein, reference 9)
	5.3 Laminar	9.3 Turbulent	
$Re_{\theta,1}$	288	845	-----
$Re_{\theta,w}$	193	433	-----
$Re_{\delta^*,1}$	913	1982	560 to 1700
$Re_{\delta^*,w}$	612	1015	-----

Apparently transition took place near the range given by Goldstein and either $Re_{\delta^*,1}$ or $Re_{\delta^*,w}$ falls into it. The lowest value of $Re_{\delta^*,1}$ computed for the bottom wall was 1160 and no laminar boundary layers were observed there.

Form parameters. - In reference 10, von Doenhoff and Tetervin suggest the usefulness of the turbulent-form parameter H_1 for defining the shape of the boundary-layer velocity profile at low speeds where compressibility is negligible. In the parameter $H_1 = \delta_1^*/\theta_1$, δ_1^* and θ_1 are the displacement and momentum thicknesses, respectively, which are computed assuming constant stream density in the boundary layer normal to the wall.

Turbulent-form parameters computed assuming a variable density in the boundary layer H and form parameters H_1 are presented in figure 8 for the bottom and side walls at the various inlet pressures. An outstanding characteristic of these plots is the constancy of the values of H_1 of 1.20 for the bottom and 1.24 for the side wall throughout the supersonic region, with the

exception of the throat region, which suggests that the velocity profile may be independent of the Mach number. The increases in H and H_1 near the throat were the result of changes in velocity profile; the irregularities in the distributions there were caused by a greater uncertainty inherent in the boundary-layer measurements because of the very small boundary-layer thicknesses and large probe flexibility.

Also included in figure 8 are theoretical values of H obtained using the theory of reference 3. The agreement between theory and experiment appears to be better at the high inlet pressures where the boundary-layer development was smooth than at the low pressures, and appears better at values of x greater than 8 inches than at values less than 8 inches. Values of H ranged from about 1.5 near the channel entrance to about 3.2 farther downstream for both experiment and theory. This large range of values is directly attributable to the compressibility of the air at high Mach numbers; the large magnitude of H at the downstream positions is attributable to the low density of the air in the boundary layer near the wall. Hence, the predominant change in the boundary-layer-profile development occurred in the density distribution.

Comparison of experimental and theoretical boundary-layer development. - A theoretical method for determining the turbulent boundary-layer development using the Kármán momentum equation is given in reference 3 and is used to predict the boundary-layer development in the two-dimensional supersonic channel investigated in this report. The following assumptions in the method are discussed:

1. No heat is transferred through the channel walls and use of a Prandtl number equal to 1 does not lead to inadmissible error in computing the boundary-layer development.
2. Empirical laws for the turbulent boundary-layer power-profile parameter and skin-friction coefficient obtained at low subsonic speeds in zero pressure gradients can be extended to supersonic flows in highly favorable pressure gradients.
3. Theoretical boundary-layer development does not affect the theoretical potential flow sufficiently to make a second calculation of the boundary-layer development necessary.
4. The pressure gradients transverse to the stream direction do not produce appreciable secondary-flow effects.

The first of these assumptions has already been considered and has been shown to have a negligible effect on the boundary-layer development and the skin-friction coefficient. The accuracy in the remaining assumptions taken collectively may be estimated by a comparison of the experimental and theoretical boundary-layer developments.

In figure 9, the experimental turbulent boundary-layer developments in terms of $\bar{\delta}$, δ^* , and θ at P_0 of 37 inches of mercury as obtained from experiment and theory (reference 3) are presented. Two theoretical developments were computed using turbulent power-profile parameters and skin-friction-coefficient laws based on $Re_{x,1}^-$ and $Re_{x,w}^-$. A comparison of these two theoretical developments with the experimental development shows that the theoretical development in which $Re_{x,w}^-$ is used to estimate the power-profile parameters and skin-friction coefficients is the better by far on both the bottom and side walls. In almost every case, the use of $Re_{x,1}^-$ gives theoretical boundary layers that are far thicker than experimental throughout the channel.

Because of its importance in determining the skin friction from profile measurements, the rate of growth of the boundary layer expressed by $\bar{\delta}$, δ^* , and θ must be considered. If the rate is included in the comparison it will be noted that even in the case of the theoretical boundary-layer development computed using $Re_{x,w}^-$ significant disagreements occur between experiment and theory. This trend is especially true on the side wall where the experimental growth near the entrance to the channel ($x < 20$ in.) is less than theoretical and farther downstream where it is greater. On the bottom wall, the reversed trend is apparent but to a lesser degree. These differences in the rate of boundary-layer growth are probably caused by secondary flows in the boundary layer and will be discussed more adequately in a later section on skin-friction coefficient.

A second calculation of the boundary-layer development was made to determine the effect of the theoretical displacement thickness on the assumed potential flow. A one-dimensional correction similar to the one employed earlier in correcting the potential-flow Mach number distribution for the presence of the experimental displacement thickness was used; the resulting corrected potential flow was used to recompute the boundary-layer development a second time. Changes in the recomputed development were less than 2 percent, indicating sufficient accuracy in using the first approximation only.

Power-profile parameter. - The power-profile parameter N , which defines the shape of the boundary-layer profile according to equation (2), was evaluated from the experimental Mach number and turbulent-form-parameter distributions along the channel length for an inlet pressure of 37 inches of mercury. The distribution of N thus obtained is presented in figure 10 for the bottom and side walls. In order to obtain N from experimental values of M_1 and H , use was made of table III of reference 3, in which N is given as a function of M_1 and H . Because N is extremely sensitive to small variations in either M_1 or H and because the variation of H with x in figure 8 is not smooth, faired values of H were used in determining N .

Empirical values of the power-profile parameter are also presented in figure 10 to be compared with the experimental points. These empirical values are given by the following formulas:

$$N_{1 \text{ or } w} = 2.6 \left(\text{Re}_{x,1 \text{ or } w}^- \right)^{1/14} \left(\frac{\frac{u}{u_\delta} - 1}{\log_e \frac{u}{u_\delta}} \right)$$

which was used in reference 3, by setting $u/u_\delta = 1$. Very little difference between N_1 and N_w is apparent for the range of Reynolds number encountered in this experiment because the exponent $1/14$ is small; hence either N_1 or N_w is equally acceptable here.

A comparison between the experimental and empirical power-profile parameters shows, in general, that the empirical values underestimate the experimental values on the bottom wall and overestimate them on the side wall. In consideration of only the proximity of the side walls, it would appear that the experimental power-profile parameter along the bottom-wall center line would be less than along the side-wall center line because the boundary layer along the bottom wall is subject to a large extent to the viscous action produced by the side walls near the channel corners. The actual behavior of the power-profile parameter, however, contradicts this supposition; the only explanation for the actual behavior appears to be in the existence of secondary flows.

Another method for determining N for the experimental profiles would be to find directly the value of N that corresponds most closely to the experimental profiles in figure 6. A selection

of a value of N corresponding to the experimental profile is difficult, however, because the experimental points actually cross several values of N , particularly for the upstream boundary layers. Only for the downstream profiles can a rational selection of N be made, and there the agreement between this new value of N with the previously determined experimental value will be good.

Skin-Friction Coefficient

Experimental skin-friction coefficients $(c_f)_1$ were computed along the wall center lines by substitution of the faired values of M_1 , δ^* , and θ presented in figures 4 and 7 into the Kármán momentum equation (reference 3) for two-dimensional flow along the bottom wall

$$\frac{d\theta}{dx} + \left[\frac{\theta (2-M_1^2) + \delta^*}{M_1 \left(1 + \frac{\gamma-1}{2} M_1^2 \right)} \right] \frac{dM_1}{dx} = \frac{\rho_w}{\rho_1} \frac{\tau}{\rho_w u_1^2} = (c_f)_1 \quad (6a)$$

and three-dimensional divergent flow along the side wall

$$\frac{d\theta}{dr} + \left[\frac{\theta (2-M_1^2) + \delta^*}{M_1 \left(1 + \frac{\gamma-1}{2} M_1^2 \right)} \right] \frac{dM_1}{dr} + \frac{\theta}{r} = \frac{\rho_w}{\rho_1} \frac{\tau}{\rho_w u_1^2} = (c_f)_1 \quad (6b)$$

The experimental friction coefficients so computed are presented in figures 11 to 13 for the bottom and side walls at P_0 of 37 to 5 inches of mercury.

Accurate calculation of skin-friction coefficients by the preceding method is difficult particularly at the low inlet pressures where considerable judgment is necessary for fairing curves for the Mach number distribution and boundary-layer development. The measurement of derivatives in equations (6a) and (6b) makes this task even more difficult. For these reasons, it was necessary to use curves that were faired near the experimental values of M and the boundary-layer development and to avoid inflection points except in the transition region of the boundary layer on the side wall at P_0 of 5 inches of mercury. Approximate average deviations in $(c_f)_1$ computed from faired and unfaired results are listed in the following table:

Inlet pressure P_0 (in.)	Deviations in $(c_f)_1$ (percent)	
	Bottom wall	Side wall
37	± 3	± 10
13	± 10	± 20
5	± 20	± 20

Friction coefficients along the bottom wall dropped severely from values averaging 0.0023 at $x = 0$ for the three inlet pressures. In contrast, more gradual drops beginning at $(c_f)_1$ of 0.0011 to 0.0016 took place on the side walls at $x = 0$. Generally, friction coefficients on the bottom wall continued to drop smoothly to $x = 44$ inches (the last position surveyed on the bottom wall); the variation along the side wall was more erratic. On the side wall a pronounced increase in $(c_f)_1$ occurred beginning at $x = 16$ inches continuing to $x = 64$ inches for P_0 of 37 inches of mercury. At P_0 of 13 inches, the side-wall skin friction tends to remain fairly constant initially with a final swing upward farther downstream. The variation of $(c_f)_1$ at P_0 of 5 inches of mercury shows the peak in $(c_f)_1$ near $x = 5$ inches taking place in the transition region and leveling off similarly to the distribution for P_0 of 13 inches of mercury, but somewhat higher.

Apparent breaks in the distribution of $(c_f)_1$ along the side walls at all three inlet pressures near $x = 32$ inches are directly attributable to the fact that the boundary-layer flow does not follow the assumed potential-flow streamlines. Such abrupt changes in $(c_f)_1$ obviously cannot exist and arise simply from elimination of the term θ/r in equation (6b) at the vertex of the test-section rhombus where r , as obtained from the theoretical potential flow, becomes infinite. Hence, a definite need exists for flow-direction measurements in boundary layers when the external potential flow is rapidly turned.

An empirical turbulent skin-friction coefficient law given first by Falkner (reference 4) is restated and its extension to high Mach numbers proposed in reference 3, where it is given as

$$(c_f)_{\bar{x},1 \text{ or } w} = \frac{0.0131}{\left[\text{Re}_{\bar{x},1 \text{ or } w} \right]^{1/7}} \quad (7)$$

Both $(c_f)_{x,1}$ and $(c_f)_{x,w}$ were used to compute the theoretical boundary-layer developments presented earlier in figure 9. Falkner gives an alternate form of the preceding law that can also be extended to depend on the kinematic viscosity at the wall as well as the stream:

$$(c_f)_{\theta,1 \text{ or } w} = \frac{0.00653}{[Re_{\theta,1 \text{ or } w}]^{1/6}} \quad (8)$$

When only stream values of the kinematic viscosity are considered, the respective coefficients are equal:

$$(c_f)_{x,1} = (c_f)_{\theta,1}$$

The coefficients based on the kinematic viscosity evaluated at the wall are related to each other by integrating equation (6a), assuming zero pressure gradient, and substituting the resulting value of x in the expression of $(c_f)_{x,w}$, equation (7). The following relation between $(c_f)_{x,w}$ and $(c_f)_{\theta,w}$ then exists:

$$(c_f)_{x,w} = (c_f)_{\theta,w} \left(\frac{\rho_w}{\rho_1} \right)^{1/6}$$

Thus by extending Falkner's formula, which is based on v_1 , to formulas based on v_w , three different values of the friction coefficient can be defined. These three values are presented in figures 11 to 13 and were computed from the experimental Reynolds numbers. In figure 13(b), laminar coefficients computed from reference 8 are presented for the region in which laminar boundary layers were observed.

In presenting the coefficients $(c_f)_{x,w}$ and $(c_f)_{\theta,w}$, a multiplying factor ρ_w/ρ_1 was included. The reason becomes evident when the right-hand side of equations (6a) and (6b) is shown in the following forms:

$$\frac{\rho_w}{\rho_1} \frac{\tau}{\rho_w u_1^2} = \frac{\rho_w}{\rho_1} (c_f)_w = \frac{\tau}{\rho_1 u_1^2} = (c_f)_1$$

The coefficients $(c_f)_w$ and $(c_f)_1$ are the skin-friction coefficients evaluated with ρ_w and ρ_1 , respectively.

A previous comparison in figure 9 involving the experimental and theoretical boundary-layer developments showed that the coefficient $(c_f)_{\bar{x},w}$ gave better results in computing the turbulent boundary-layer development than $(c_f)_{\bar{x},1}$. A comparison of $(c_f)_{\bar{x},w}$ and $(c_f)_{\theta,w}$ shows only slight differences, and it may therefore be concluded that either of these coefficients is suitable for computing the theoretical turbulent development.

Comparisons of the experimental and empirical skin-friction coefficients show agreement in orders of magnitude only and display considerable differences in detailed variations along the channel. The extremely high values of $(c_f)_1$ near $x = 0$ in figures 11(a) and 12(a) for the bottom wall are in sharp contrast to the empirically predicted values and to the experimental and empirical coefficients found in the same region on the side walls (figs. 11(b) and 12(b)). Likewise the fair agreement between experiment and empiricism for the bottom wall farther downstream contrasts with the poor agreement downstream on the side wall where the experimental coefficients begin to rise despite the continued increases in Reynolds number.

The good agreement between experiment and theory in the boundary-layer development using the empirical skin-friction law based on the wall kinematic viscosity (fig. 9) as distinguished from the poor agreement between the experimental and empirical skin-friction coefficients can be explained on the basis of differences in the rate of boundary-layer growth. One of the factors used in evaluating the experimental friction coefficients is the rate of growth $d\theta/dx$ and $d\theta/dr$ in equations (6a) and (6b). Also, an analysis of figures 9 and 11 shows that, for regions in which the experimental boundary-layer growth is more rapid than that predicted by the method of reference 3, the friction coefficients are likewise higher than empirical and vice versa. This analysis considers, of course, only the theoretical developments and friction coefficients involving $(c_f)_{\bar{x},w}$ because those based on stream values of the kinematic viscosity departed too far from experiment. Because the discrepancies in the experimental and theoretical boundary-layer growths were believed to be the result of secondary-flow effects and because skin-friction and boundary-layer development are directly related, the same explanation would follow for the discrepancies between the experimental and empirical friction coefficients.

The theoretical laminar friction coefficients shown in figure 13(b) compare reasonably well with the measured values in view of the low-accuracy characteristic of the measurements of the thin laminar boundary layers.

Secondary Flows

In both the theoretical analysis of the boundary-layer development (reference 3) and in the present experimental analysis, the implicit assumption has been made that in the boundary layer no flow occurs across planes normal to the wall and oriented in the direction of the potential flow, that is, that secondary flows are negligible. This assumption is known to be invalid for flows having static-pressure gradients transverse to these planes (reference 9); the error introduced by neglecting secondary flows may account for the disagreement between experiment and theory and the various other anomalies observed in the analysis of the experimental results.

Any nozzle flow will have the following characteristics:

(a) The streamlines of the flow outside the boundary layer will tend to follow along the predicted potential flow streamlines; and
(b) the streamlines of the flow in the boundary-layer will tend to follow the static-pressure gradient. In all such nozzles, with the exception of axially symmetric ones, these characteristics will give rise to secondary flows in the boundary layer corresponding approximately to the secondary-flow pattern sketched in figure 14. The static-pressure distributions p/P_0 along the side and bottom walls causing these secondary flows are presented in the same figure and are taken from the theoretically computed potential flow.

In the transonic and initial expansion region of the supersonic nozzle, the boundary layer tends to flow toward the top and bottom walls; and in the straightening region, toward the center line of the side walls. Such transverse flow of low-energy air may account for some of the disagreements between experiment and theory in the boundary-layer developments presented earlier. This flow would cause the retarded rate of boundary-layer growth near the entrance and the accelerated growth farther downstream on the channel-side-wall center line and the reversed behavior on the bottom wall previously noted. Also, the low values of power-profile parameter N observed on the greater part of the side wall compared with the higher values on the bottom wall suggest a transport of low-energy air toward the center line of the side wall.

More detailed analyses of other peculiarities observed, such as the great differences in Mach number between the side and bottom walls in the test section at low pressures, the presence of laminar boundary layers on the side walls and turbulent boundary layers on the bottom wall near the channel entrance, and higher Mach numbers in the presence of greater boundary-layer thicknesses, cannot be expected without specific research into secondary flows.

The existence of secondary flows as previously described indicates that flow-direction measurements are necessary to determine the extent of the three-dimensional character of the boundary-layer flow. If the flow departs appreciably from the assumed two-dimensional form, momentum equations (6a) and (6b) are no longer applicable for computing skin-friction coefficients. For channels having higher Mach numbers than the one investigated herein, the pressure gradients will be larger and the secondary-flow phenomena will become more serious.

SUMMARY OF RESULTS

Boundary-layer measurements were made in a two-dimensional channel designed by potential-flow methods for a uniform, test-section Mach number of 2.08. Investigations at inlet pressures of 5, 13, and 37 inches of mercury absolute gave the following results:

1. The Mach number distribution throughout the channel and the boundary-layer-profile development were almost independent of the inlet pressure in the range from 37 to 21 inches of mercury. From 13 to 5 inches of mercury, substantial changes in the Mach number distribution and boundary-layer development took place.
2. Wall-surface temperature-recovery factors were approximately $1\frac{1}{2}$ percent lower than theoretical recovery factors for insulated surfaces with turbulent boundary layers.
3. Turbulent-boundary-layer profiles were found throughout the channel at all inlet pressures with the exception of the entrance region of the side wall at an inlet total pressure of 5 inches of mercury.
4. The best approximation of the boundary-layer velocity profiles to power-law profiles occurred in regions of zero pressure gradient.

1384
5. Transition of the boundary layer from laminar to turbulent on the side wall occurred within the range of Reynolds number of 913 to 1982 based on boundary-layer displacement thickness and kinematic viscosity evaluated in the stream. This transition is within the range commonly accepted. No laminar layers were observed on the bottom wall and Reynolds numbers there were higher than on the side wall.

6. Turbulent-form parameters computed assuming constant stream density in the boundary layer remained constant at 1.20 for the bottom and 1.24 for the side wall throughout the channel for all inlet pressures except in the region of the throat where these values increased. Turbulent-form parameters computed with variable density in the boundary layer varied from approximately 1.5 near the channel entrance to 3.2 in the test section. The predominant change in the boundary-layer-profile development occurred in the density distribution with relatively small changes in the velocity distribution.

7. The magnitude of the experimental boundary-layer development at an inlet total pressure of 37 inches of mercury agreed well with the theoretical magnitude when turbulent skin-friction coefficients based on the kinematic viscosity of the air at the wall were used. The principal discrepancy between experiment and theory was in the rate of the boundary-layer development, which was probably caused by secondary flows in the boundary layer. Because the present theory does not take secondary flows into account, a precise check between theory and experiment should not be expected.

8. In general, the experimental power-profile parameters were higher than empirical on the bottom wall and lower on the side wall.

9. Empirical coefficients using Reynolds numbers based on the kinematic viscosity at the wall appeared to conform more closely to experiment than those using Reynolds numbers based on the kinematic viscosity in the stream. A discontinuity in the distribution of these coefficients along the side wall was attributed to large deviations in the radius of streamline curvature from the assumed potential flow. Such deviations indicate the need for flow-direction measurements in addition to conventional boundary-layer pressure measurements for experimentally determining friction coefficients

in flows with pressure gradients. The disagreement between the experimental and empirical friction coefficients was probably caused by secondary flows in the boundary layer.

Lewis Flight Propulsion Laboratory,
National Advisory Committee for Aeronautics,
Cleveland, Ohio, April 28, 1950.

APPENDIX - SYMBOLS

The following symbols are used in this report:

$(c_f)_l$	local coefficient of friction based on density evaluated at stream edge of boundary layer, $\tau/\rho_l u_l^2$
$(c_f)_w$	local coefficient of friction based on density evaluated at wall, $\tau/\rho_w u_l^2$
$(c_f)_{\bar{x},l}$	empirical local coefficient of friction based on $Re_{\bar{x},l}$ and density evaluated at stream edge of boundary layer
$(c_f)_{\bar{x},w}$	empirical local coefficient of friction based on $Re_{\bar{x},w}$ and density evaluated at wall
$(c_f)_{\theta,l}$	empirical local coefficient of friction based on $Re_{\theta,l}$ and density evaluated at stream edge of boundary layer
$(c_f)_{\theta,w}$	empirical local coefficient of friction based on $Re_{\theta,w}$ and density evaluated at wall
H	turbulent-form parameter assuming variable density in boundary layer, δ^*/θ
H_i	turbulent-form parameter assuming constant stream density in boundary layer, δ_i^*/θ_i
M	Mach number
N	power-profile parameter, $\frac{u}{u_\delta} = \left(\frac{y}{\delta}\right)^{1/N}$
P	total pressure, absolute
Pr	Prandtl number
p	static pressure, absolute
$Re_{\bar{x},l}$	Reynolds number based on equivalent length of run and kinematic viscosity evaluated at stream edge of boundary layer
$Re_{\bar{x},w}$	Reynolds number based on equivalent length of run and kinematic viscosity evaluated at wall

$Re_{\theta,l}$ Reynolds number based on momentum thickness and kinematic viscosity evaluated at stream edge of boundary layer

$Re_{\theta,w}$ Reynolds number based on momentum thickness and kinematic viscosity evaluated at wall

r apparent radius of radial flow

T temperature

u velocity

$u_{\overline{\delta}}$ $0.99 u_1$

x distance downstream of geometric nozzle throat

\overline{x} equivalent length of turbulent run

y distance normal to wall

γ ratio of specific heats

δ boundary-layer thickness

$\overline{\delta}$ boundary-layer thickness at $u_{\overline{\delta}}$

δ^* displacement thickness assuming variable density in

boundary layer,
$$\int_0^{\delta} \left(1 - \frac{\rho u}{\rho_1 u_1} \right) dy$$

δ_1^* displacement thickness assuming constant stream density

in boundary layer,
$$\int_0^{\delta} \left(1 - \frac{u}{u_1} \right) dy$$

η_r temperature recovery factor

θ momentum thickness assuming variable density in boundary

layer,
$$\int_0^{\delta} \frac{\rho u}{\rho_1 u_1} \left(1 - \frac{u}{u_1} \right) dy$$

θ_1 momentum thickness assuming constant stream density in

boundary layer,
$$\int_0^{\delta} \frac{u}{u_1} \left(1 - \frac{u}{u_1} \right) dy$$

ν kinematic viscosity of air

ρ density

τ shear stress at wall

Subscripts:

0 value taken in surge chamber

1 value taken at stream edge of boundary layer

w value taken at wall

REFERENCES

1. Foelsch, Kuno: A New Method of Designing Two-Dimensional Laval Nozzles for a Parallel and Uniform Jet. Rep. No. NA-46-235-2, Thermodynamics Sec., Eng. Dept., North American Aviation, Inc., May 27, 1946.
2. Liepmann, Hans Wolfgang, and Puckett, Allen E.: Introduction to Aerodynamics of a Compressible Fluid. John Wiley & Sons, Inc., 1947.
3. Tucker, Maurice: Approximate Turbulent Boundary-Layer Development in Plane Compressible Flow along Thermally Insulated Surfaces with Application to Supersonic-Tunnel Contour Correction. NACA TN 2045, 1950.
4. Falkner, V. M.: A New Law for Calculating Drag. Aircraft Eng., vol. XV, no. 169, March 1943, pp. 65-69.
5. Squire, H. B.: Heat Transfer Calculation for Aerofoils. R. & M. No. 1986, British A.R.C., Nov. 1942.
6. Tribus, Myron, and Boelter, L. M. K.: An Investigation of Aircraft Heaters. II - Properties of Gases. NACA ARR, Oct. 1942.

7. Wilson, R. E., Young, E. C., and Thompson, M. J.: 2nd Interim Report on Experimentally Determined Turbulent Boundary Layer Characteristics at Supersonic Speeds. CM-501 DRL-196, Defense Res. Lab., Univ. Texas, Jan. 25, 1949. (Bur. Ord. Contract NOrd-9195.)
8. Kármán, Th., and Tsien, H. S.: Boundary Layer in Compressible Fluids. Jour. Aero. Sci., vol. 5, no. 6, April 1938, pp. 227-232.
9. Goldstein, Sidney: Modern Development in Fluid Dynamics. Vol. I. Clarendon Press (Oxford), 1938, pp. 84-87, 326-327.
10. von Doenhoff, Albert E., and Tetervin, Neal: Determination of General Relations for the Behavior of Turbulent Boundary Layers. NACA Rep. 772, 1943.

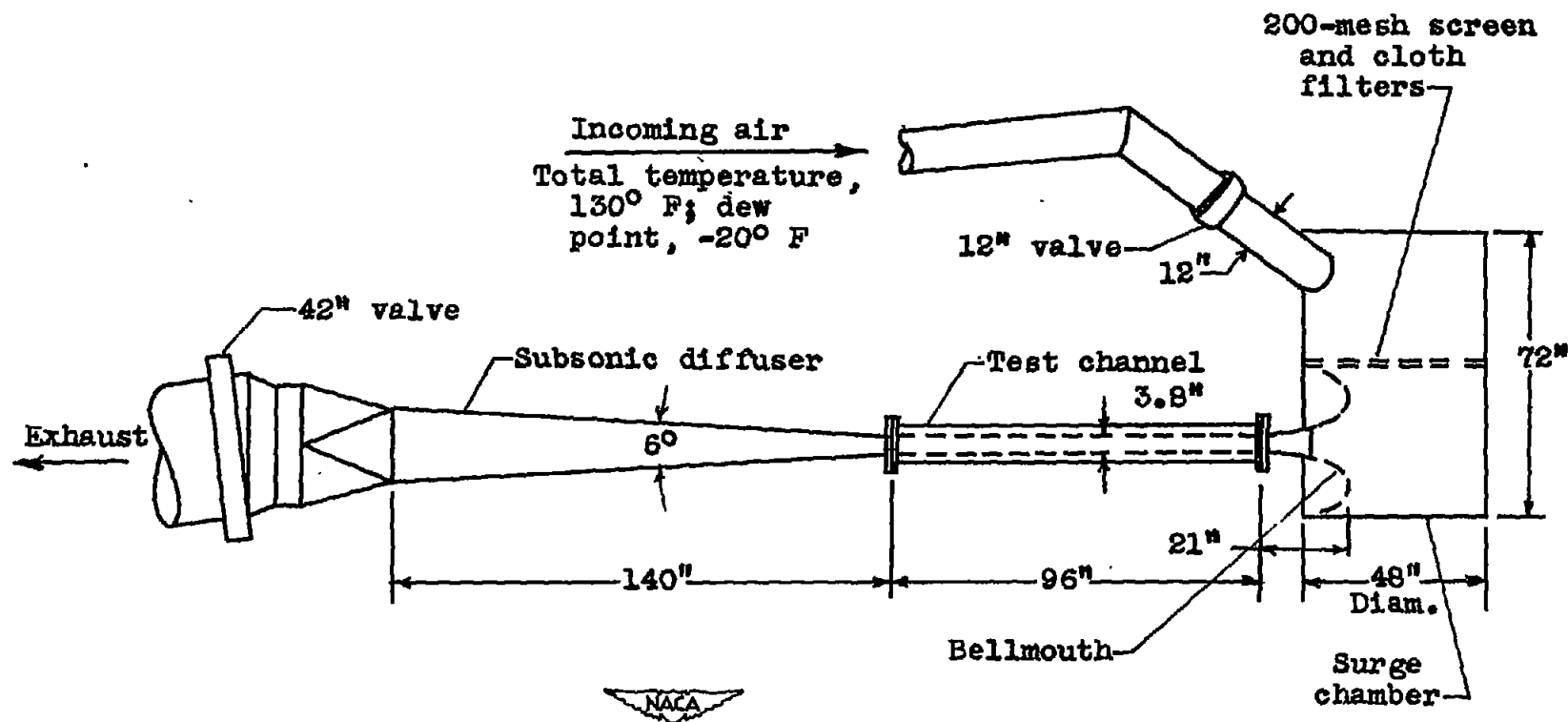
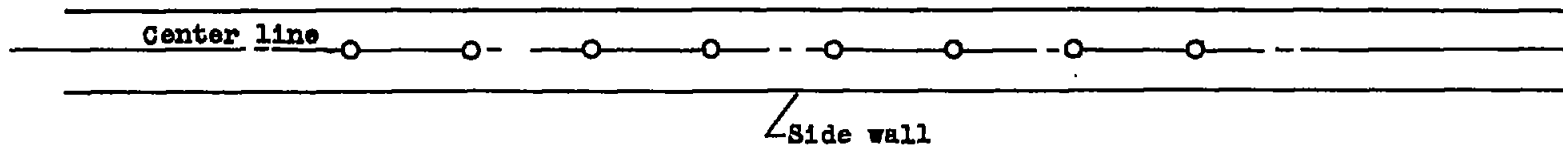


Figure 1. - 3.84- by 10-inch test channel and auxiliary piping (plan view).

- Point at which boundary-layer survey was made
- + Point at which inside-wall-surface temperature was measured



View A-A of bottom wall (looking down)

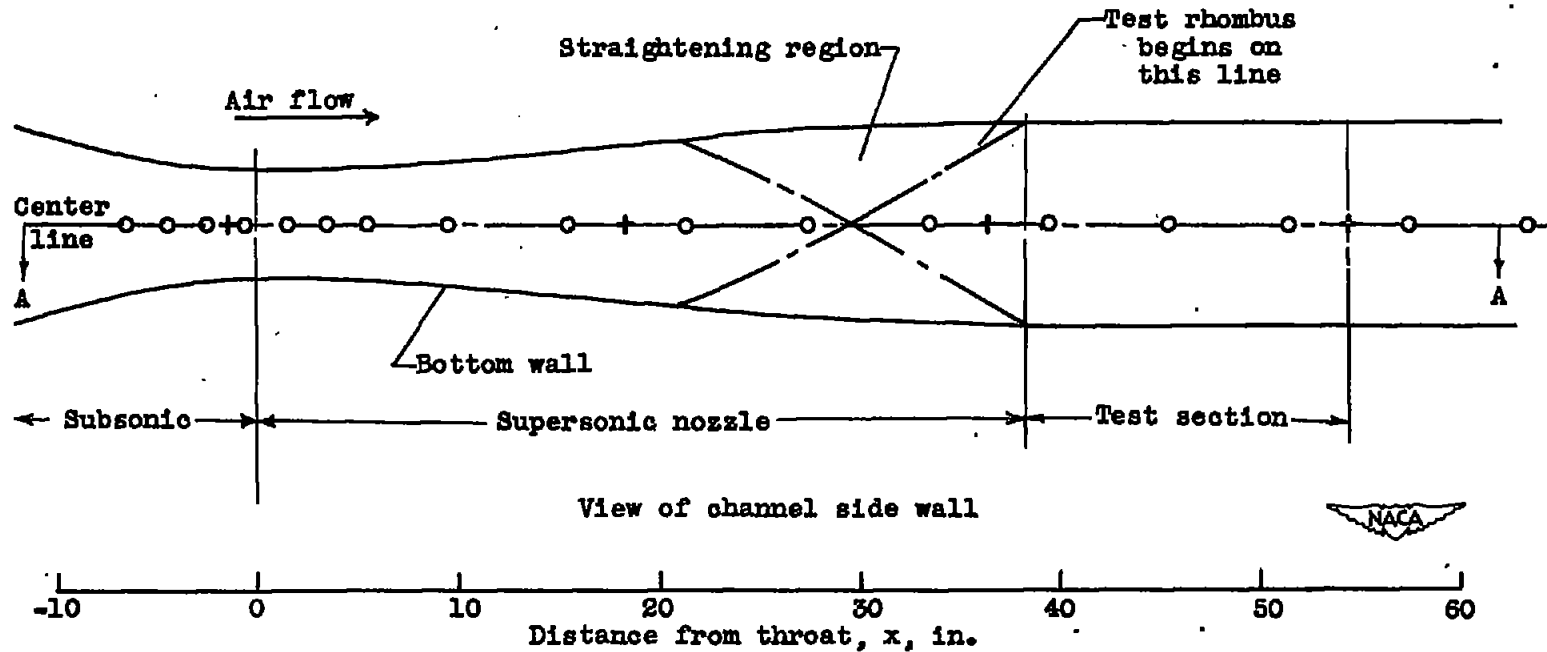
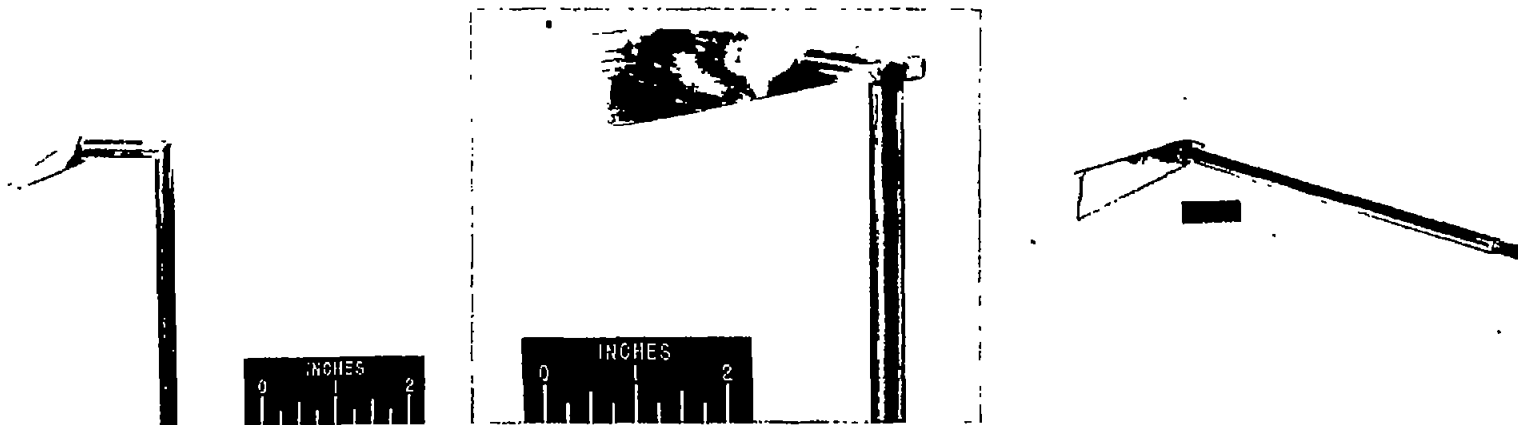


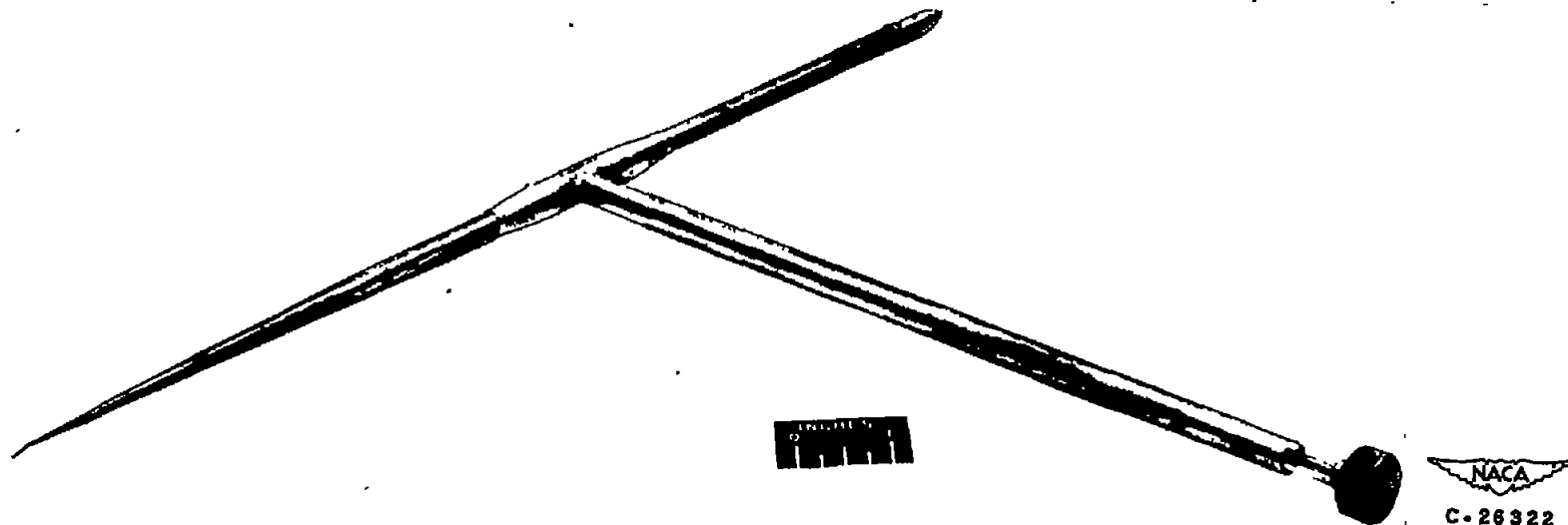
Figure 2. - Test-channel instrumentation.



(a) Probe a.

(b) Probe b.

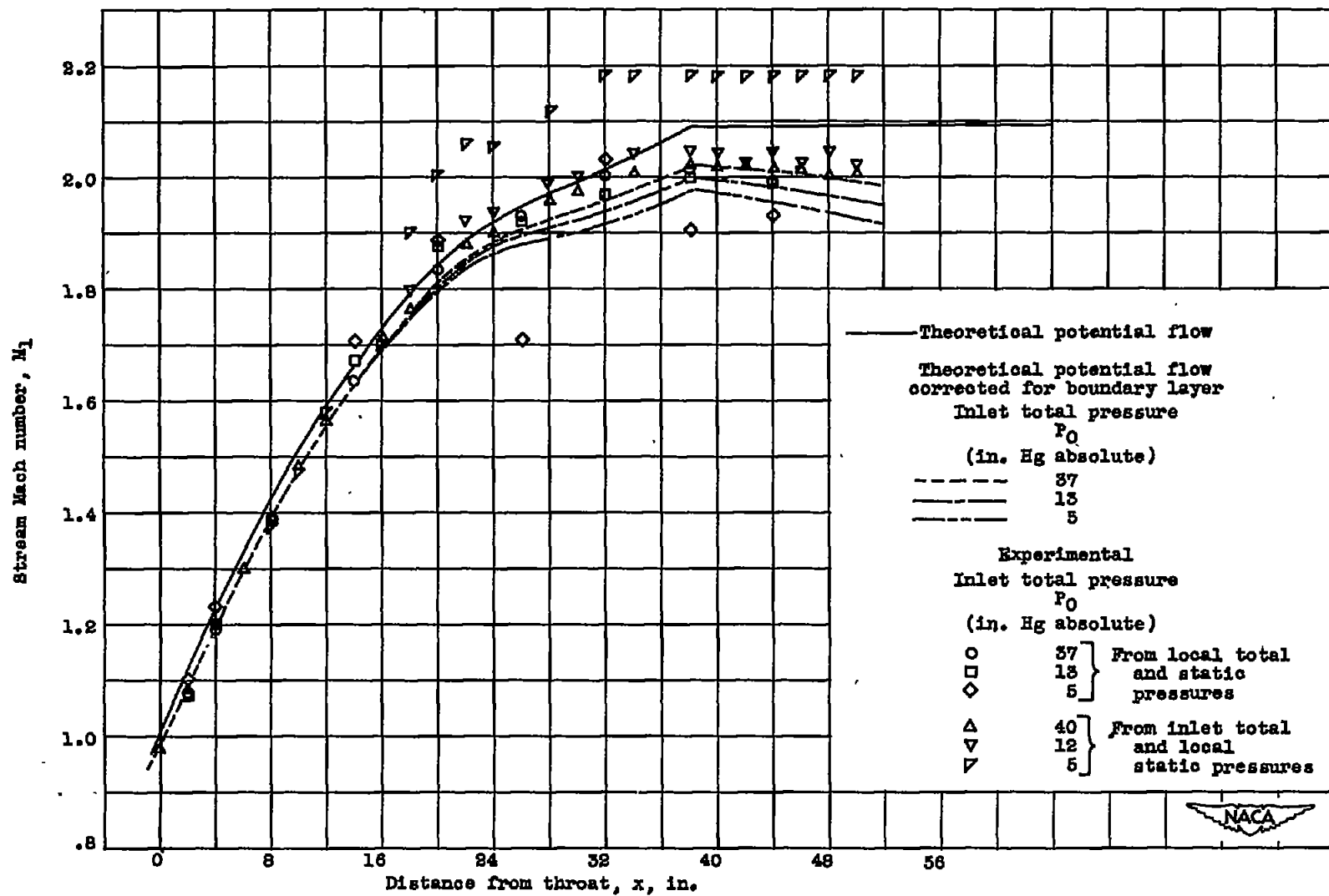
(c) Probe c.



(d) Probe d.

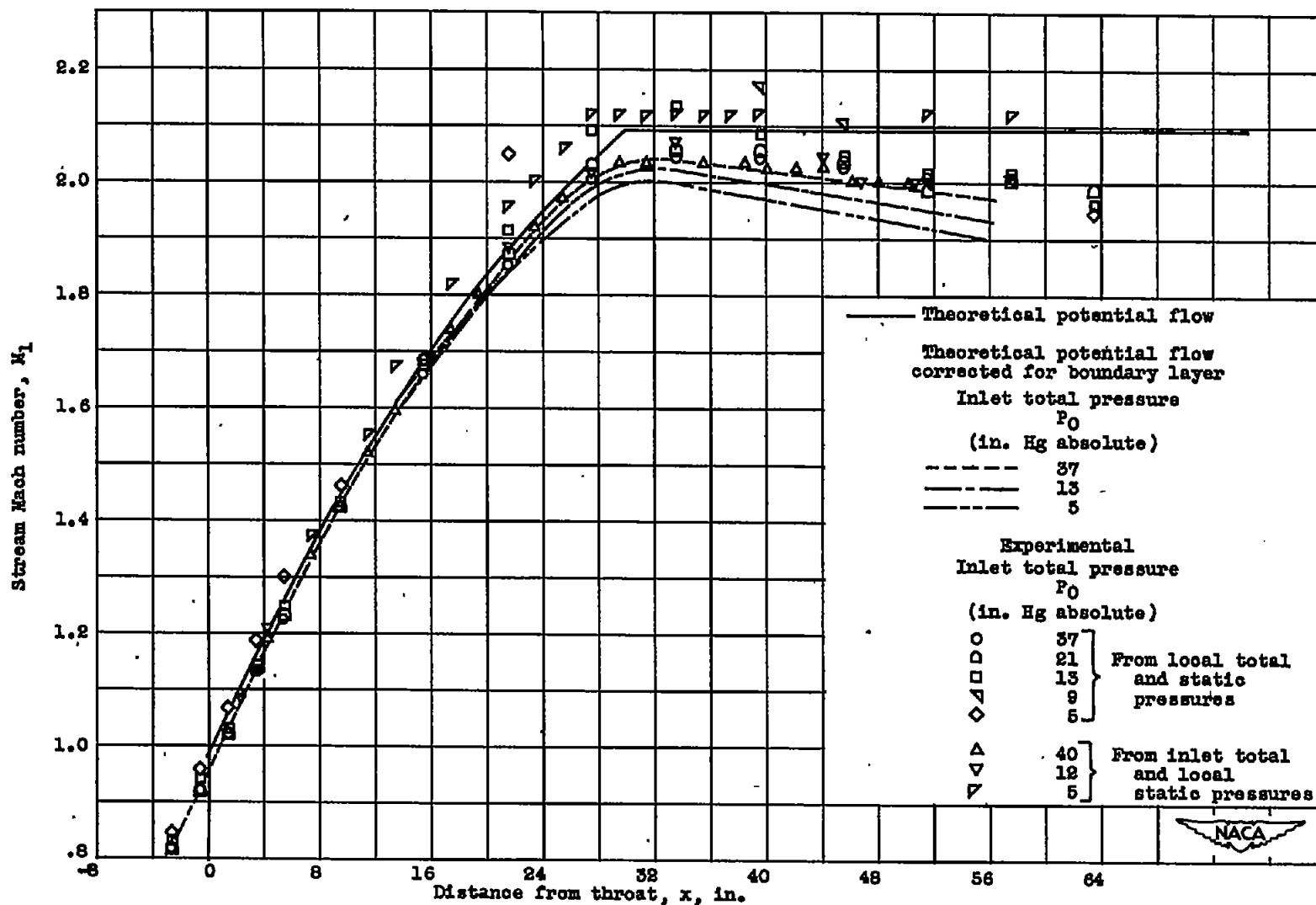
Figure 3. - Pressure probes.

NACA
C-26322



(a) Along center line of bottom wall of channel.

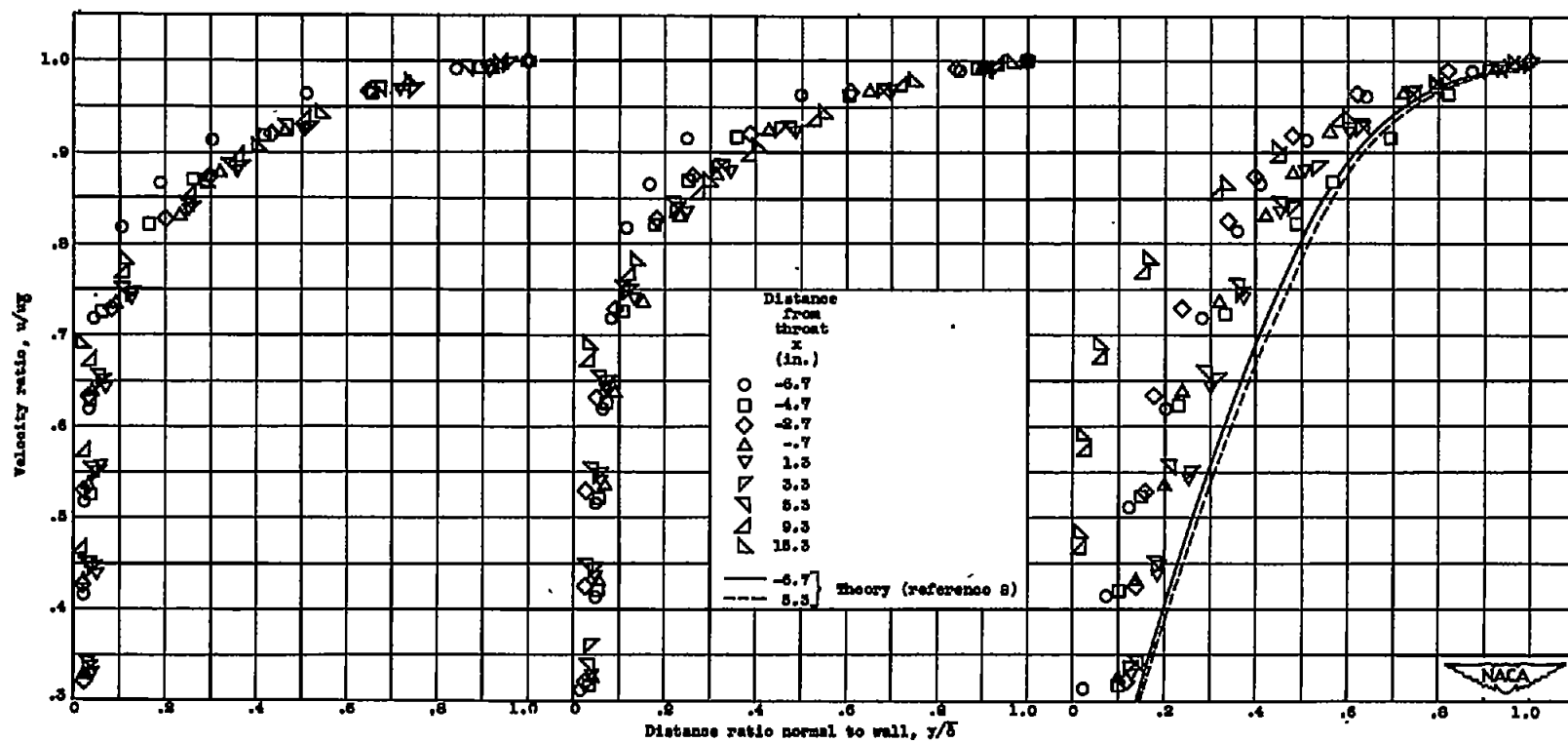
Figure 4. - Mach number distribution.



(b) Along center line of side wall of channel.

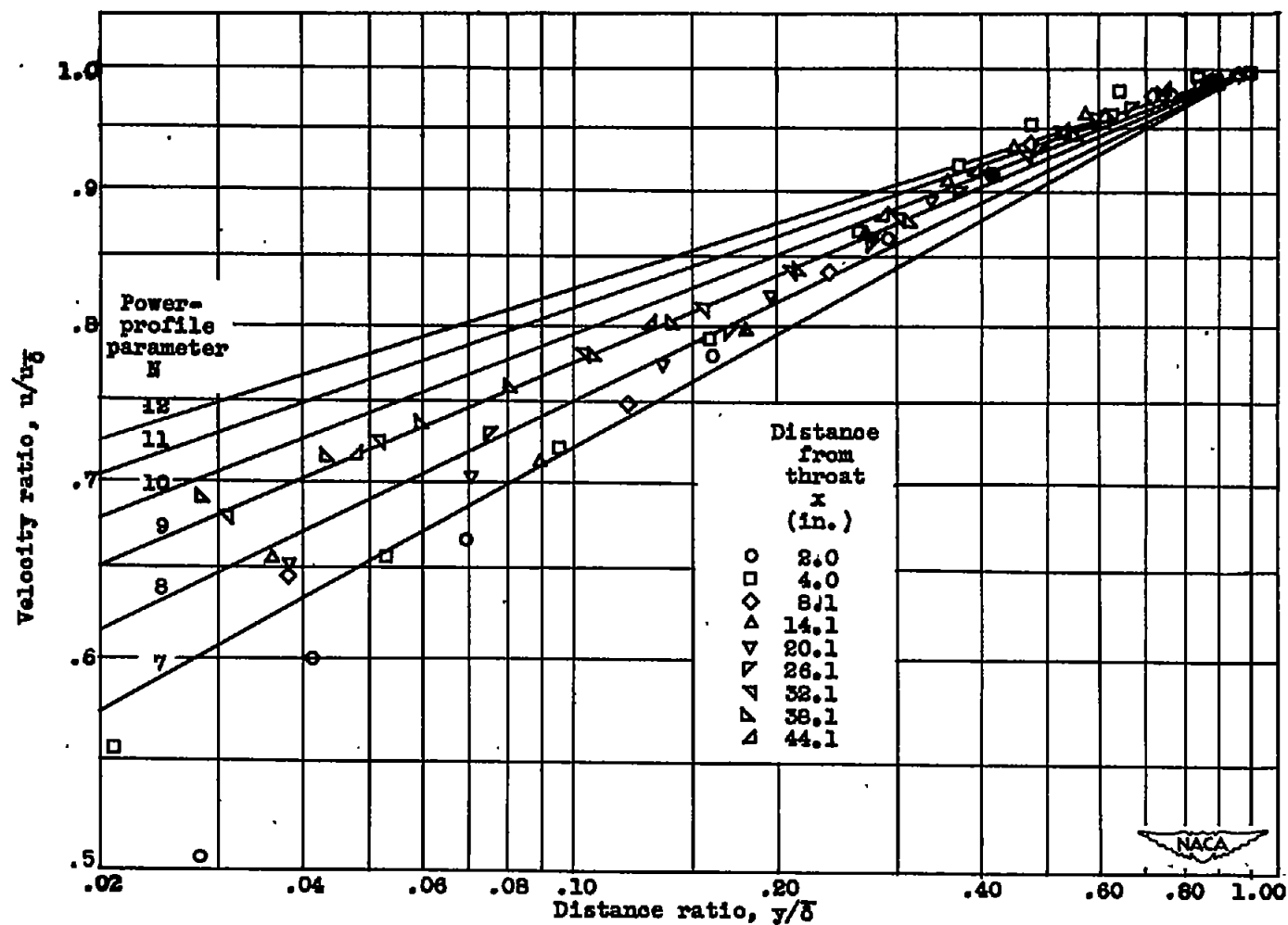
Figure 4. - Concluded. Mach number distribution.

1384



(a) Inlet pressure, 37 inches of mercury absolute. (b) Inlet pressure, 13 inches of mercury absolute. (c) Inlet pressure, 5 inches of mercury absolute.

Figure 8. - Nondimensional boundary-layer-velocity profiles in transonic-flow region of channel along center line of side wall. Range of free-stream Mach number, 0.87 to 1.68.



(a) Center line of bottom wall.

Figure 6. - Boundary-layer profiles on side and bottom walls at inlet pressure of 37 inches of mercury.

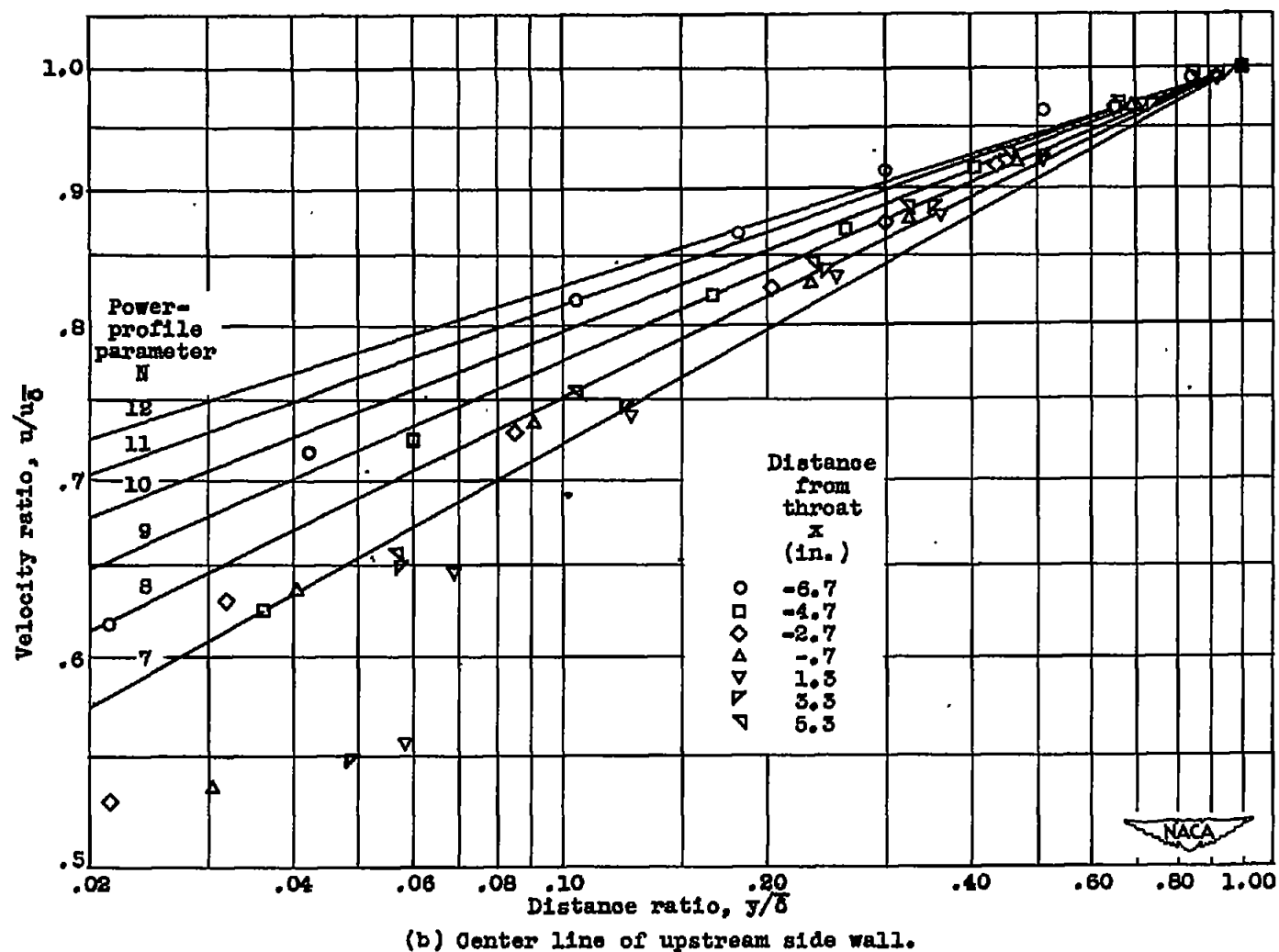
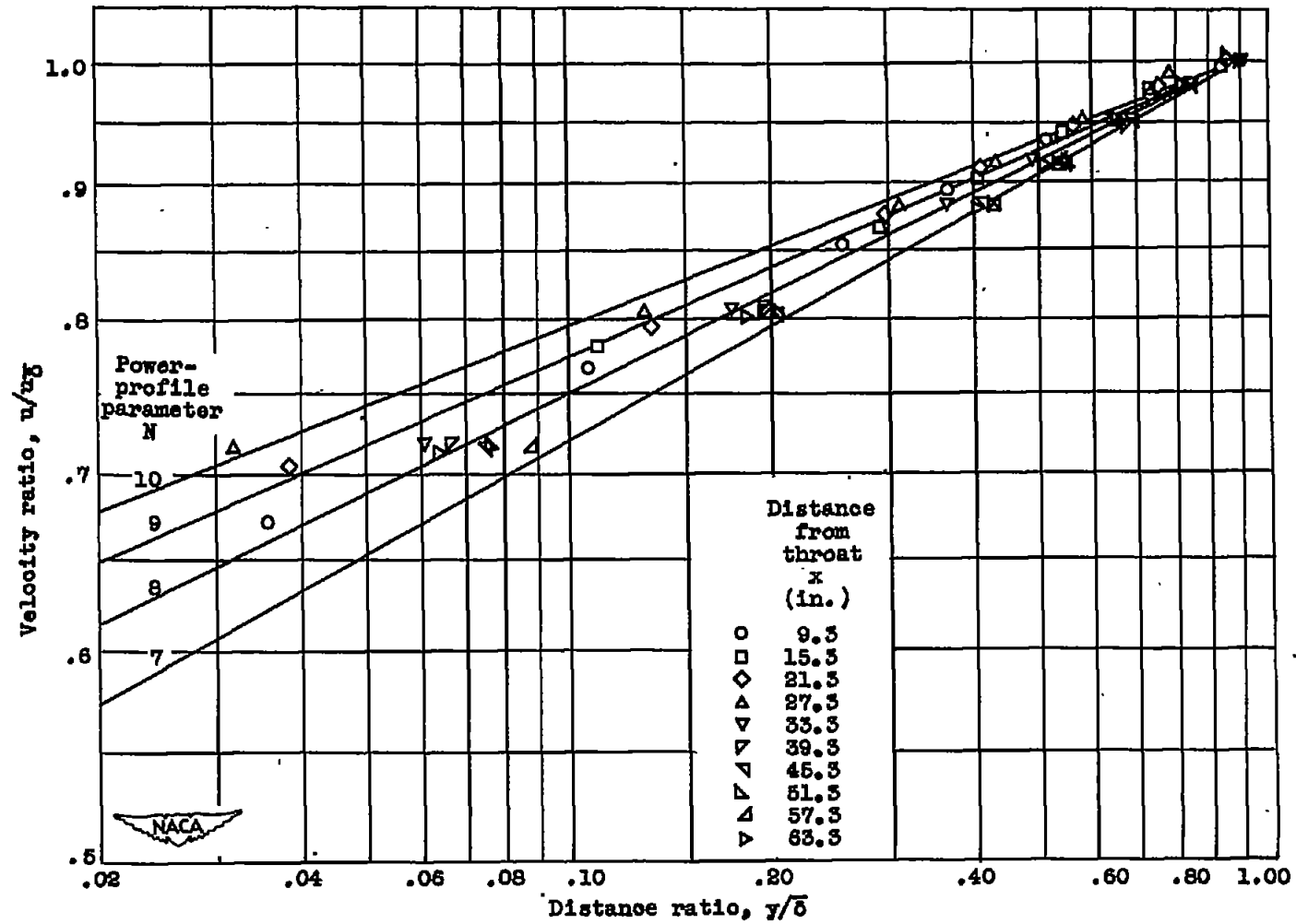
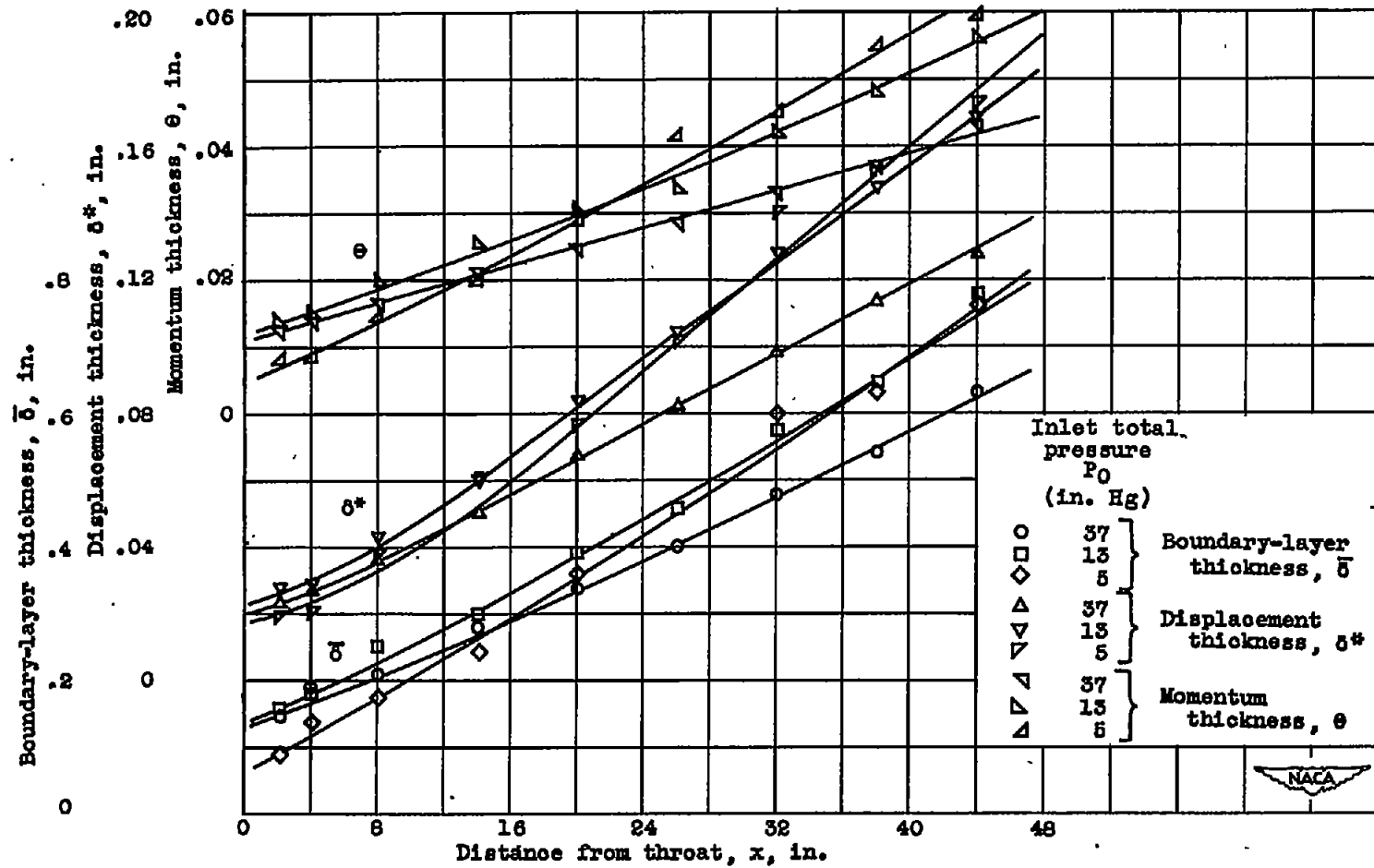


Figure 6. - Continued. Boundary-layer profiles on side and bottom walls at inlet pressure of 37 inches of mercury.



(c) Center line of downstream side wall.

Figure 6. - Concluded. Boundary-layer profiles on side and bottom walls at inlet pressure of 37 inches of mercury.



(a) Center line of bottom wall.

Figure 7. - Boundary-layer development along channel.

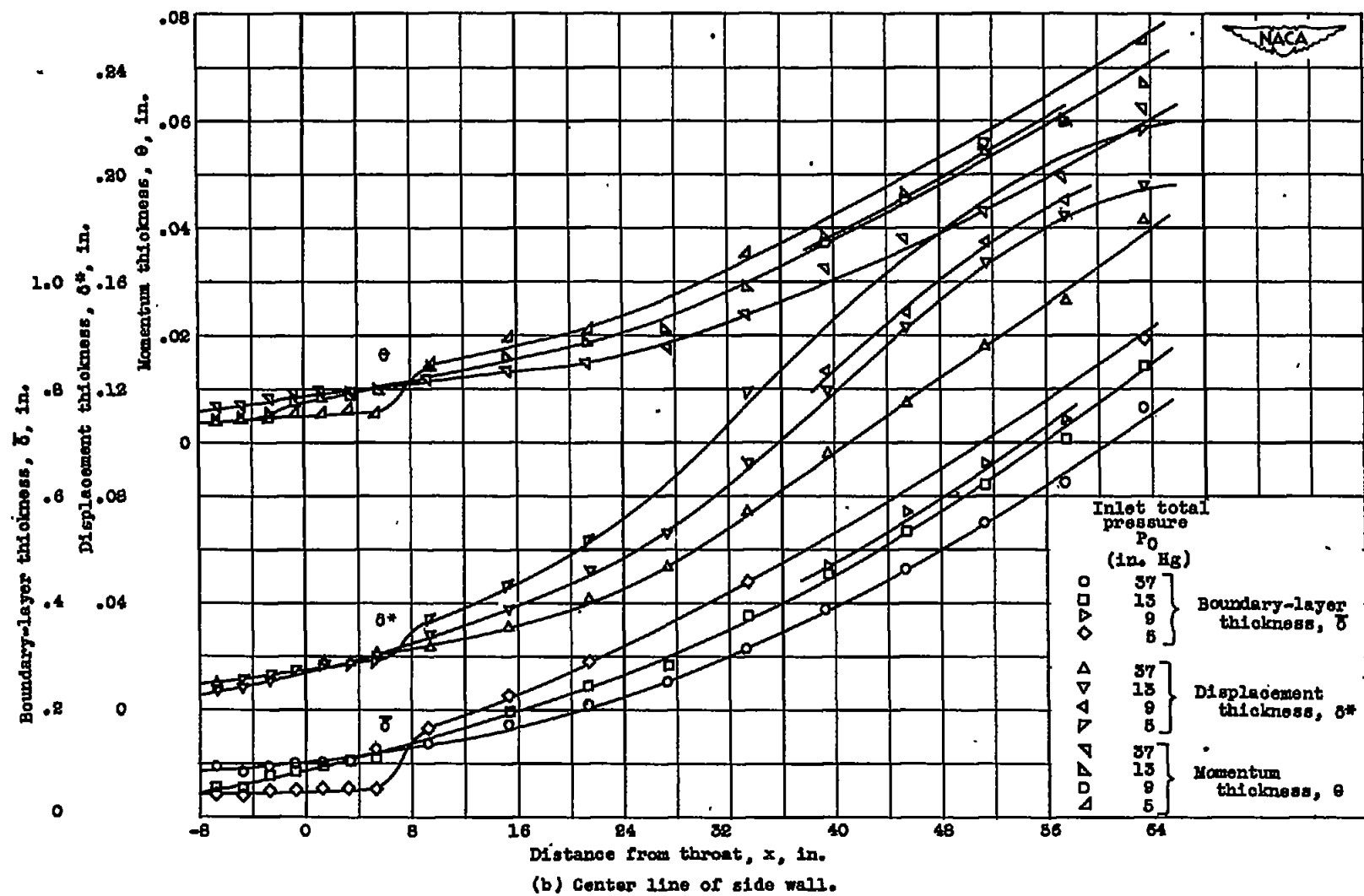
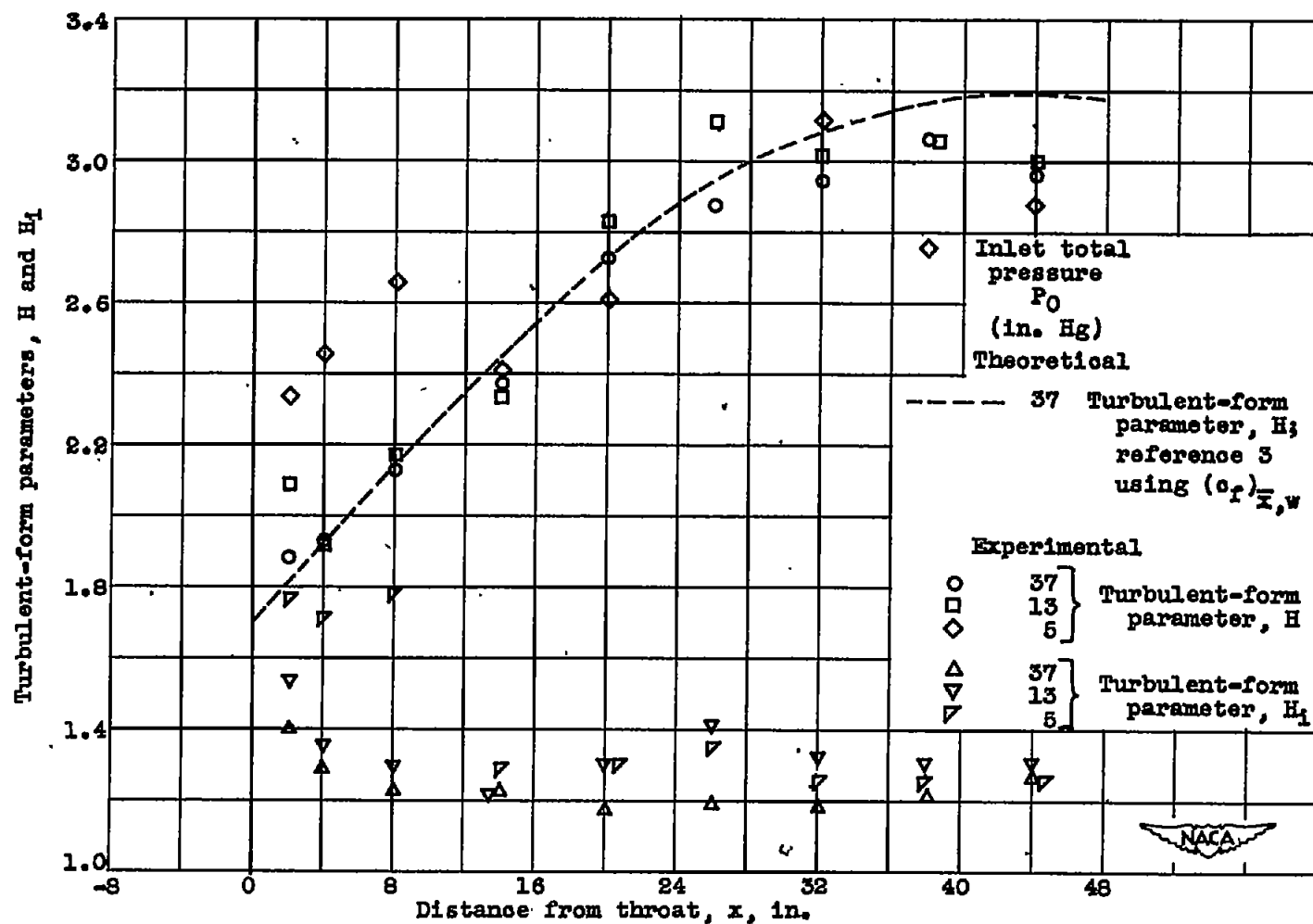
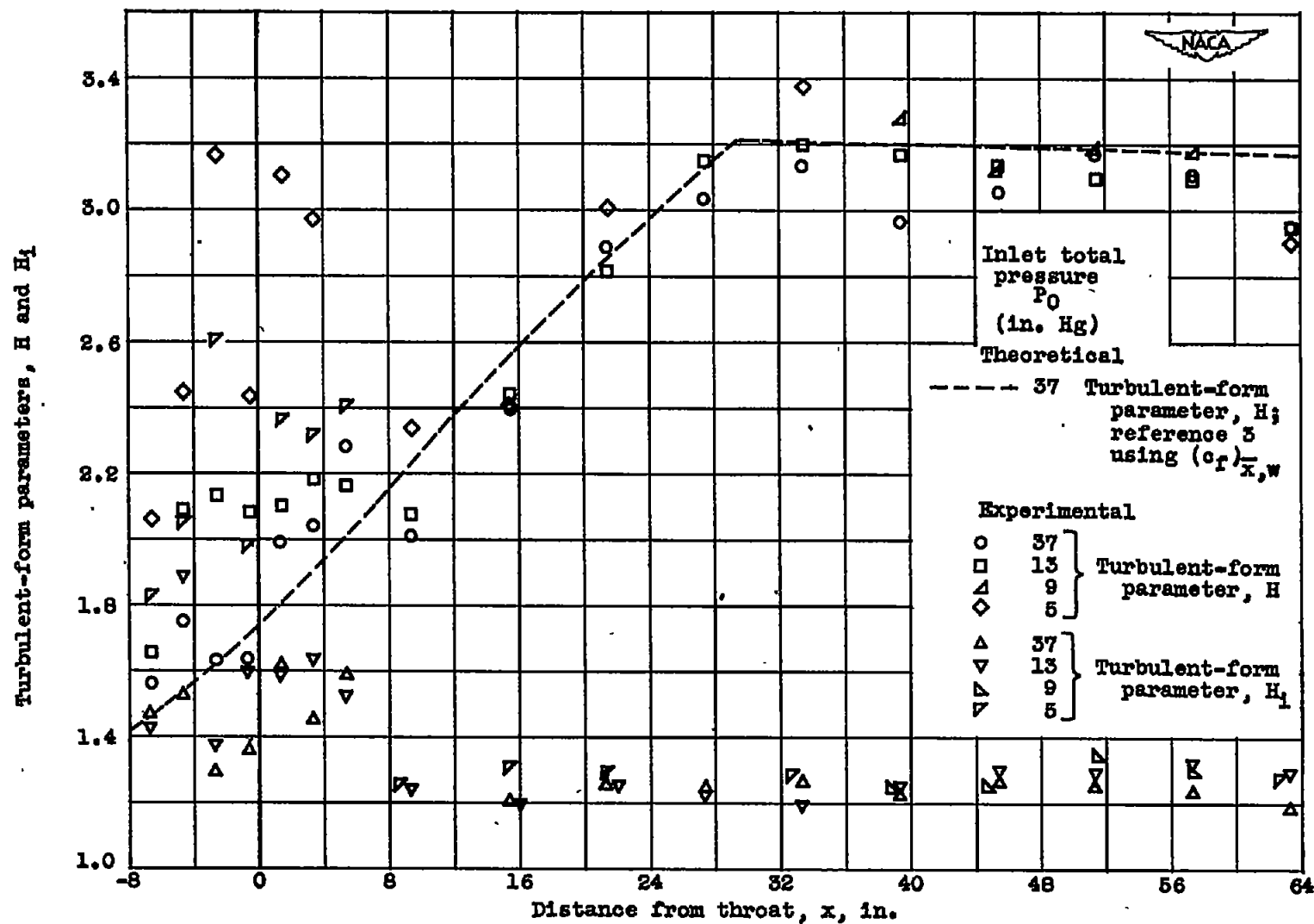


Figure 7. - Concluded. Boundary-layer development along channel.



(a) Along center line of bottom wall of channel.

Figure 8. - Turbulent-form-parameter variation.



(b) Along center line of side wall of channel.

Figure 8. - Concluded. Turbulent-form-parameter variation.

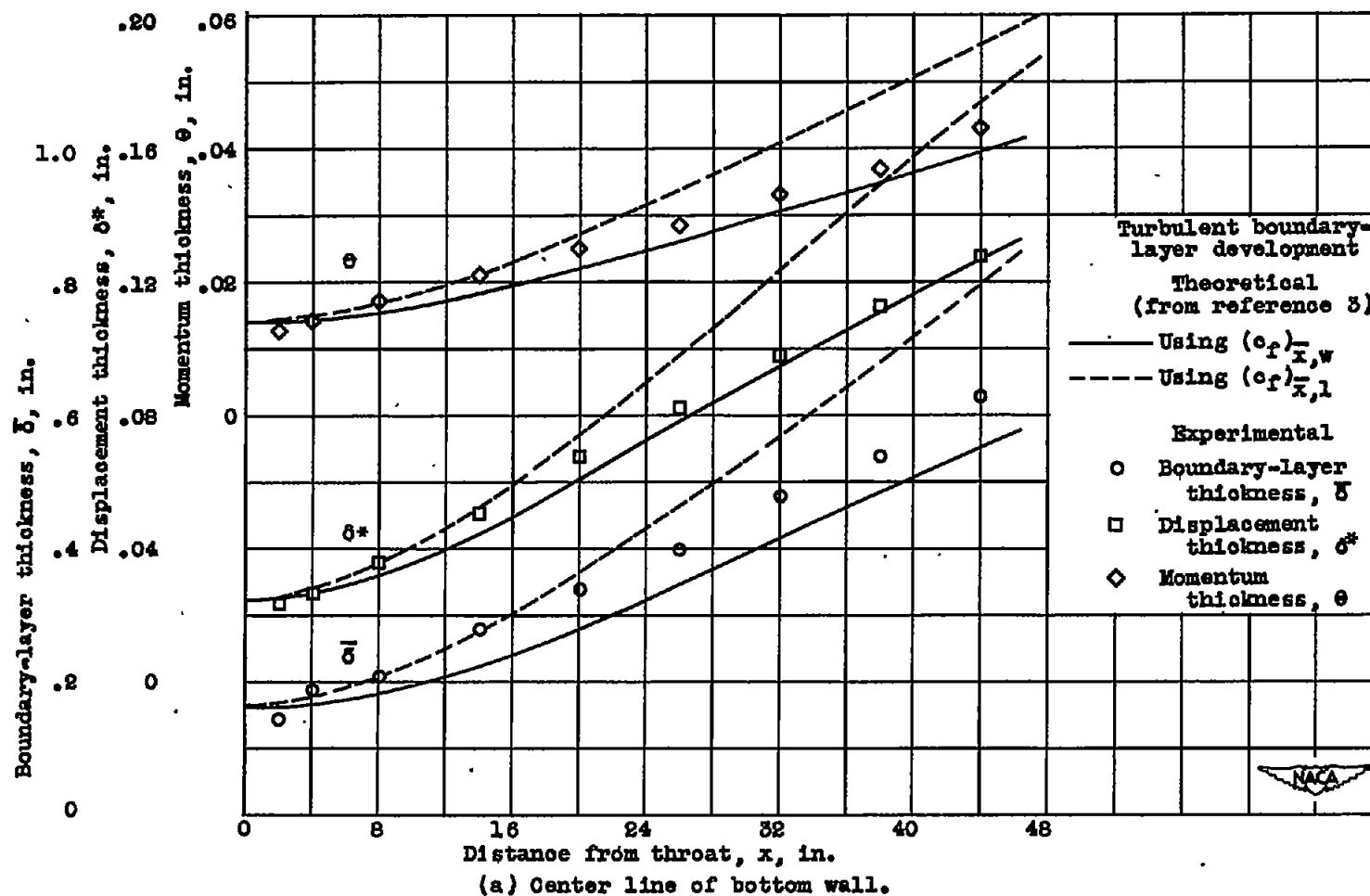


Figure 9. - Comparison of experimental and theoretical boundary-layer development along channel at inlet pressure of 37 inches of mercury.

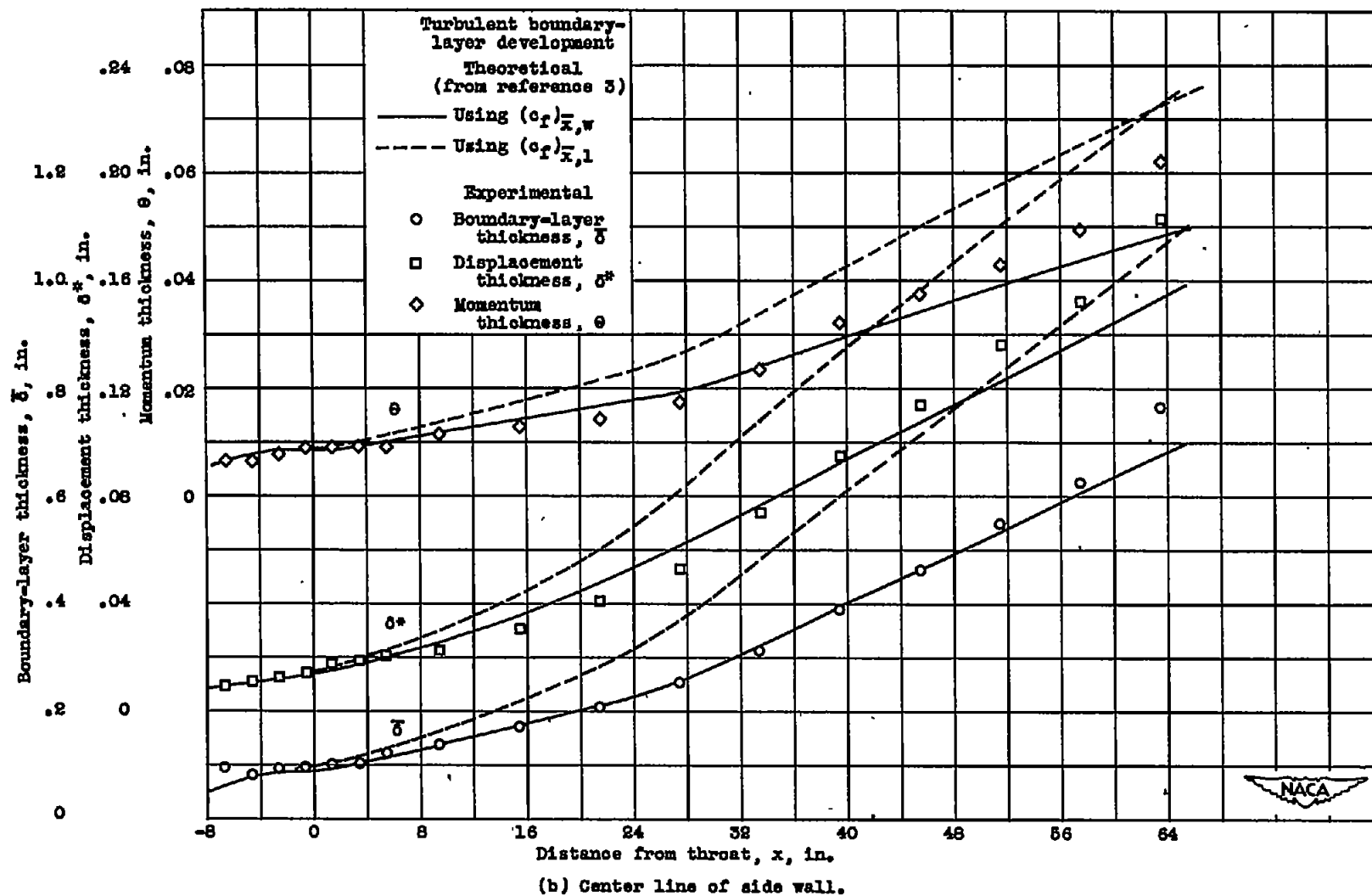
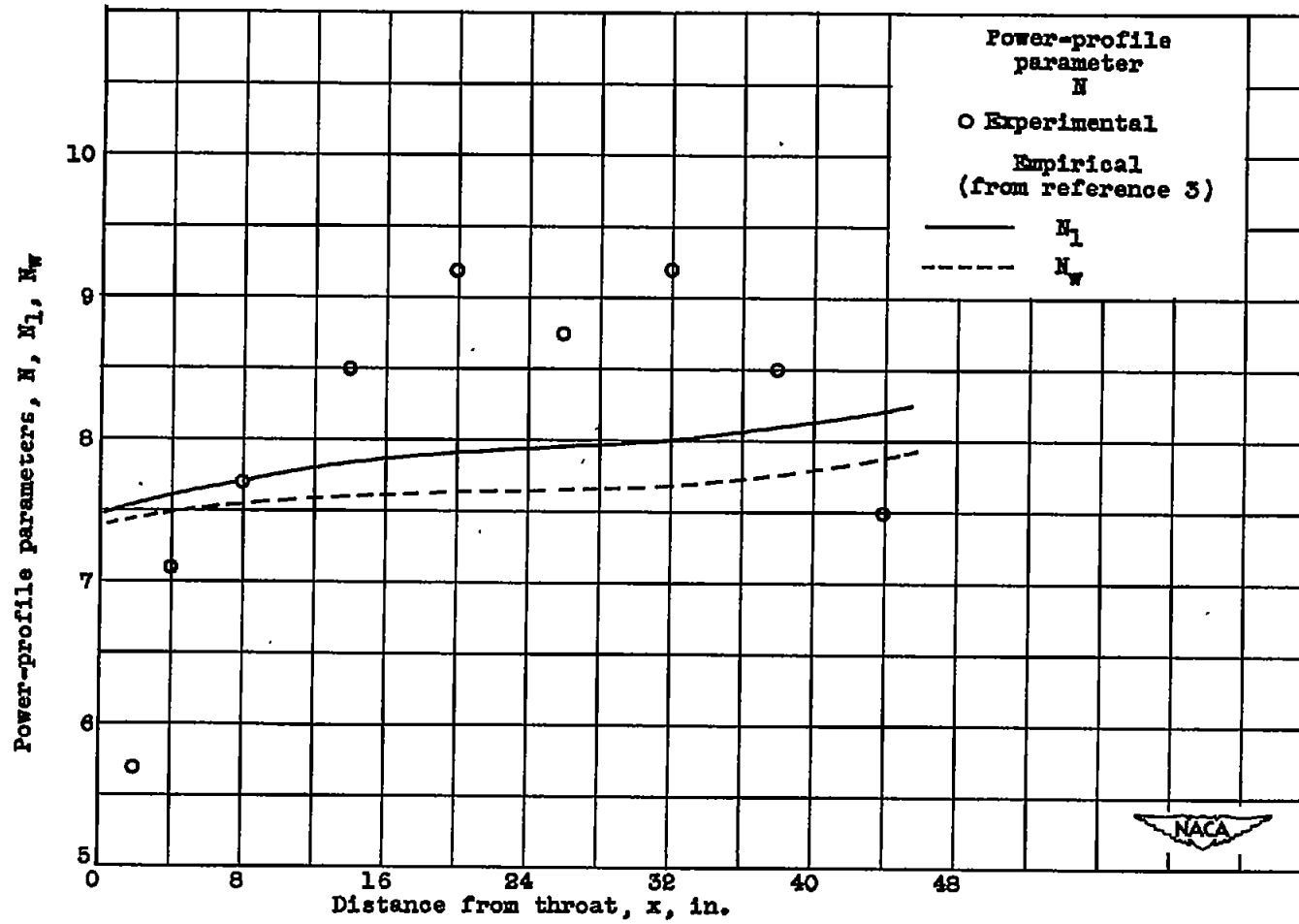


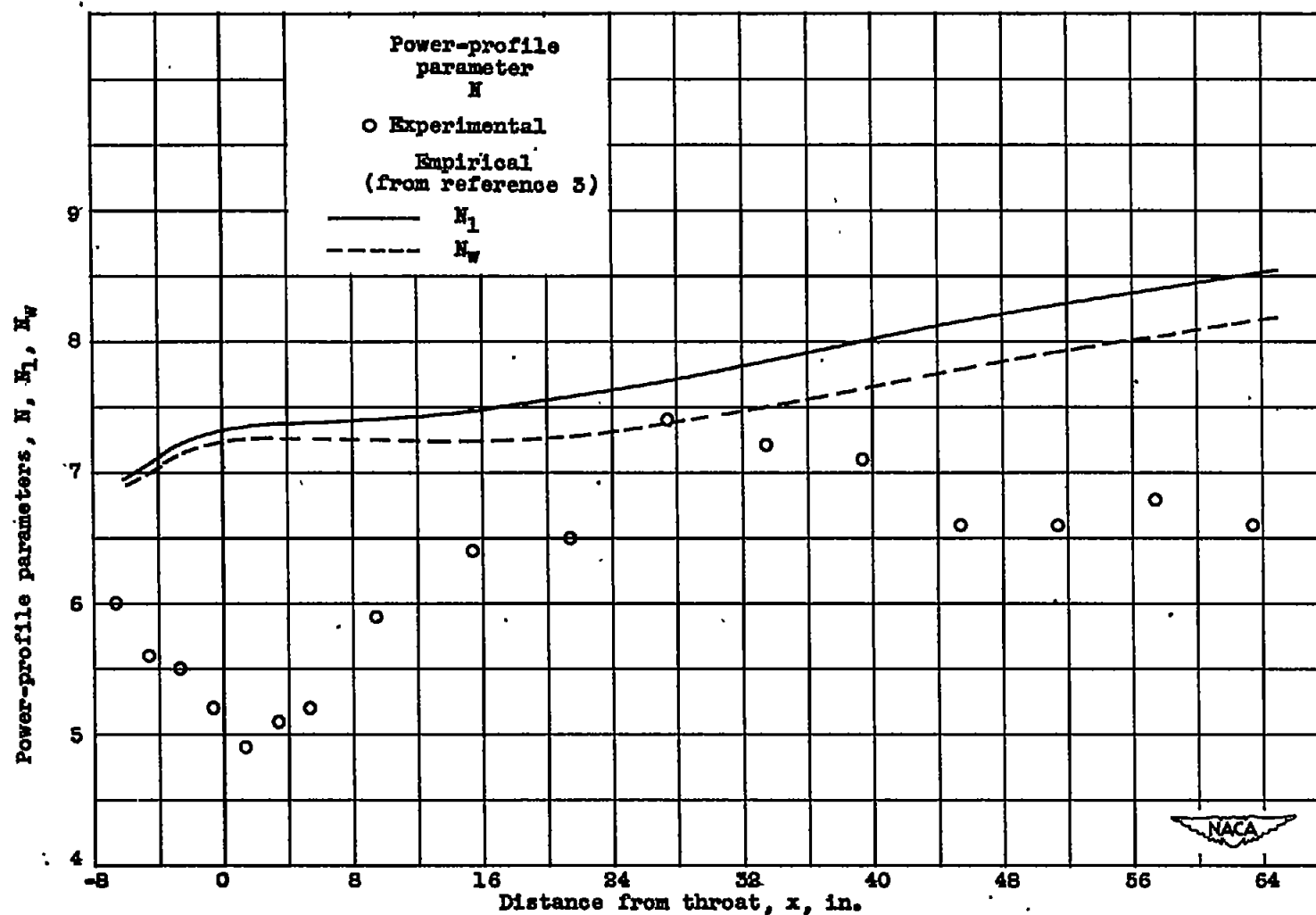
Figure 9. - Concluded. Comparison of experimental and theoretical boundary-layer development along channel at inlet pressure of 37 inches of mercury.

1384



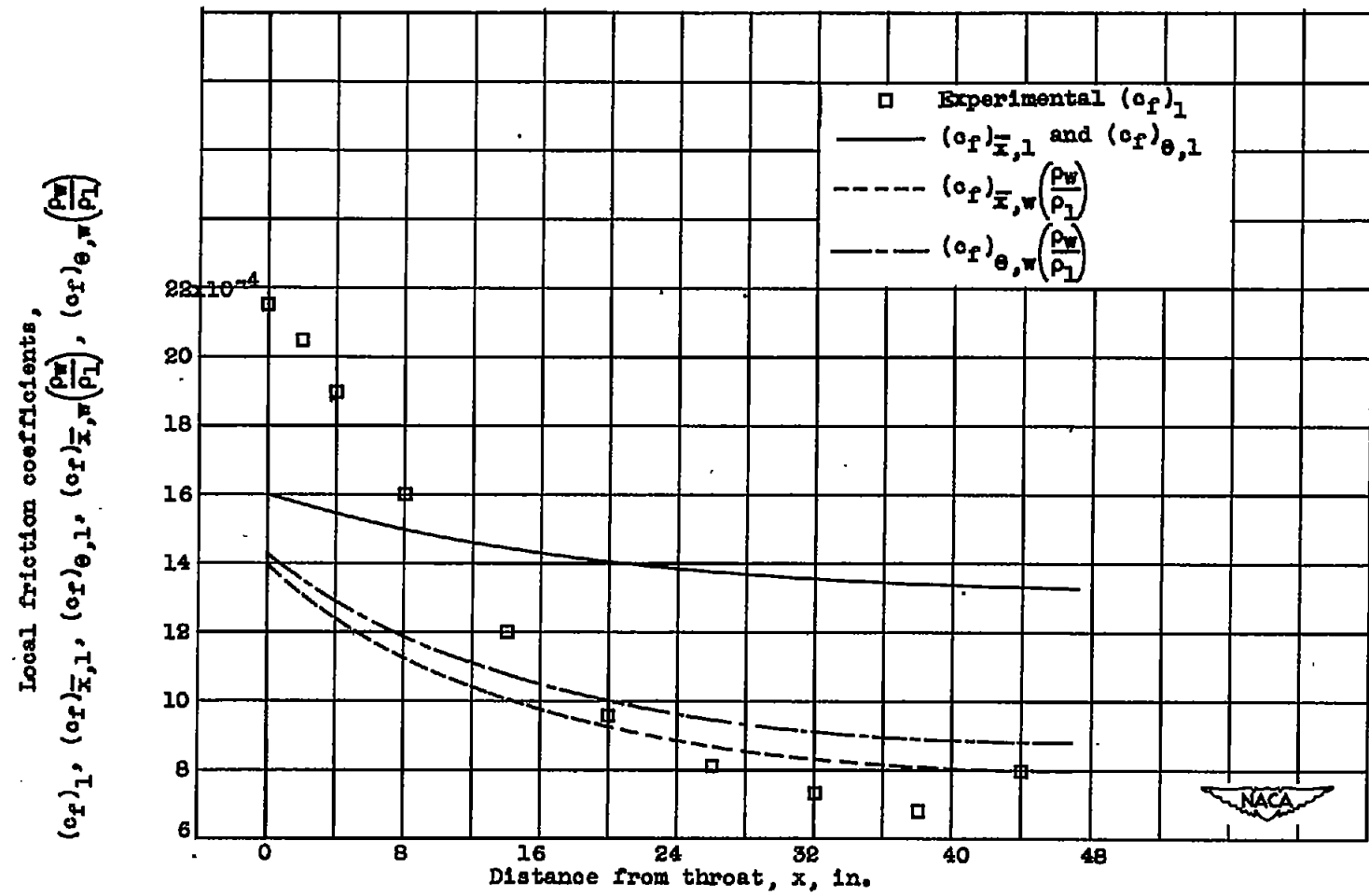
(a) Center line of bottom wall.

Figure 10. - Comparison of experimental and empirical power-profile parameters along channel at inlet pressure of 37 inches of mercury.



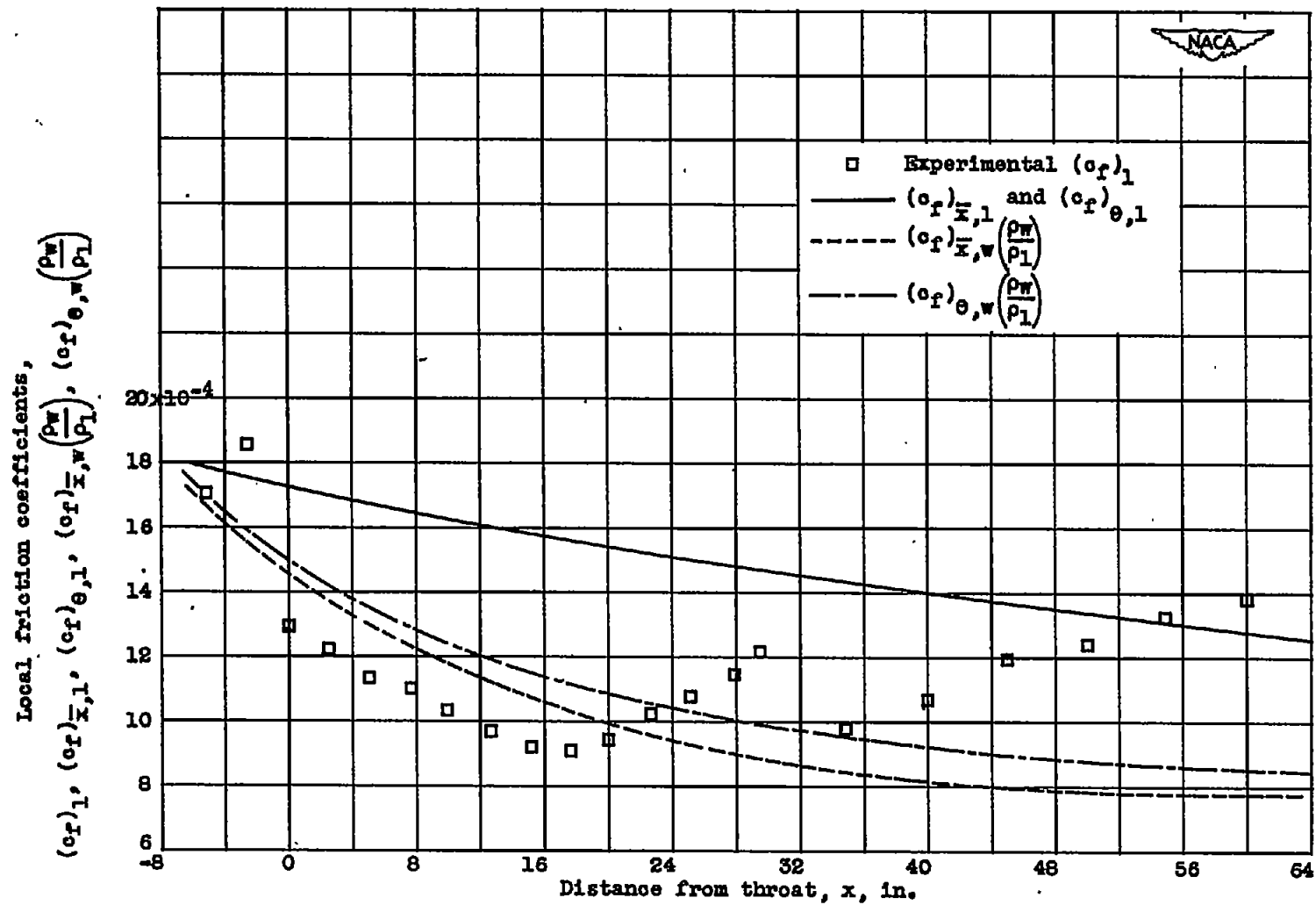
(b) Center line of side wall.

Figure 10. - Concluded. Comparison of experimental and empirical power-profile parameters along channel at inlet pressure of 37 inches of mercury.



(a) Center line of bottom wall.

Figure 11. - Comparison of experimental and empirical skin-friction coefficients along channel at inlet pressure of 37 inches of mercury.



(b) Center line of side wall.

Figure 11. - Concluded. Comparison of experimental and empirical skin-friction coefficients along channel at inlet pressure of 37 inches of mercury.

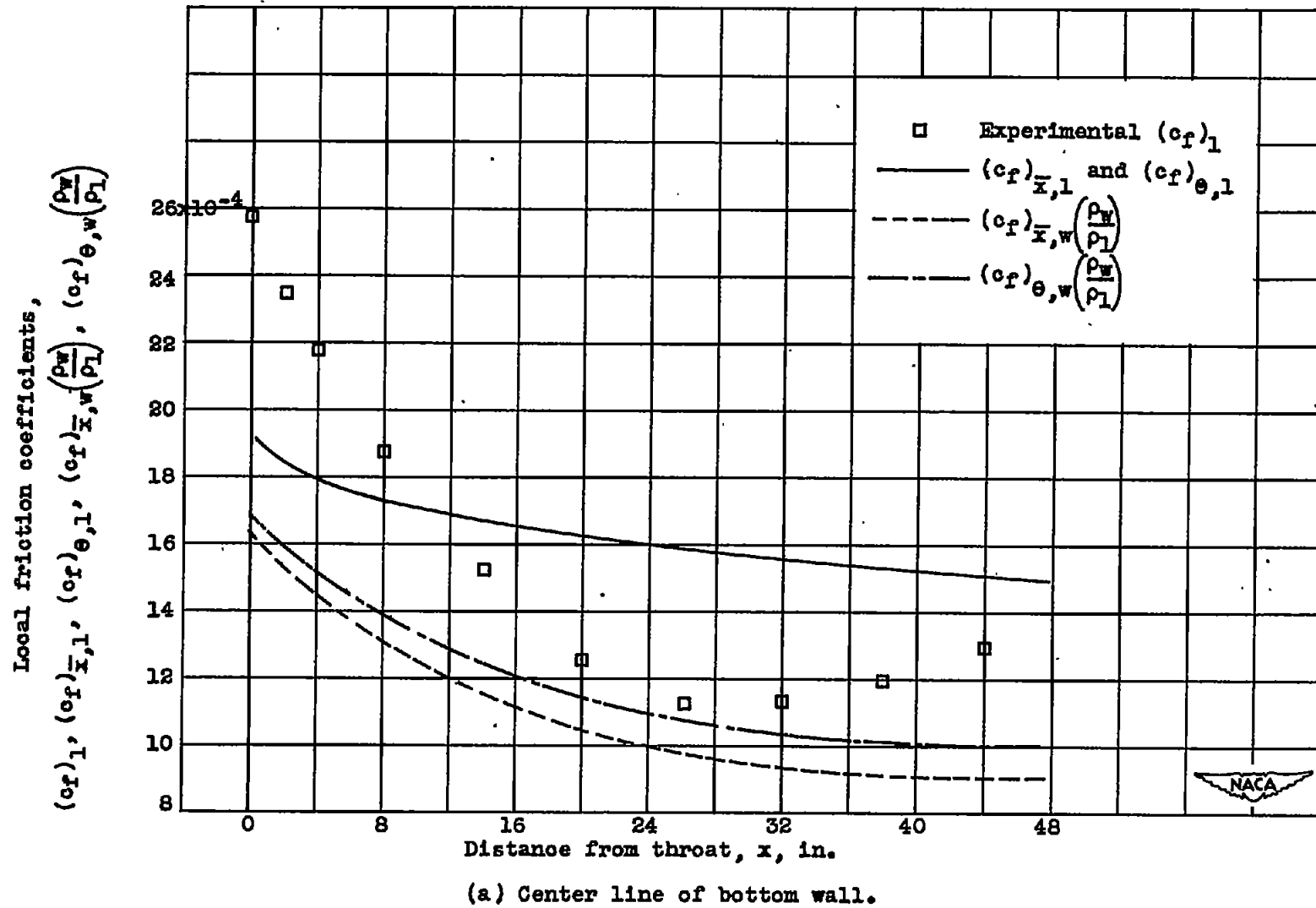
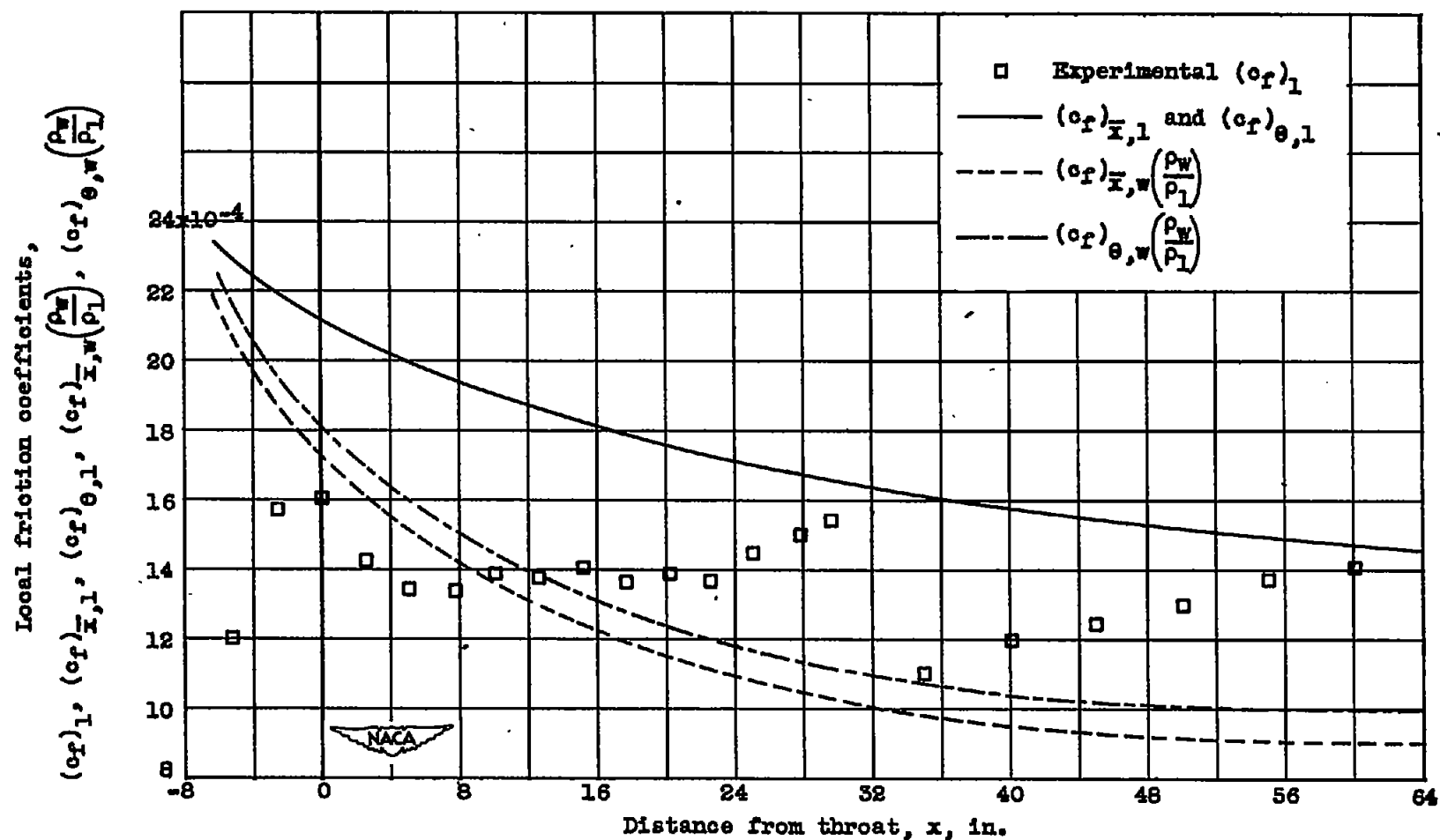


Figure 12. - Comparison of experimental and empirical skin-friction coefficients along channel at inlet pressure of 13 inches of mercury.



(b) Center line of side wall.

Figure 12. - Concluded. Comparison of experimental and empirical skin-friction coefficients along channel at inlet pressure of 13 inches of mercury.

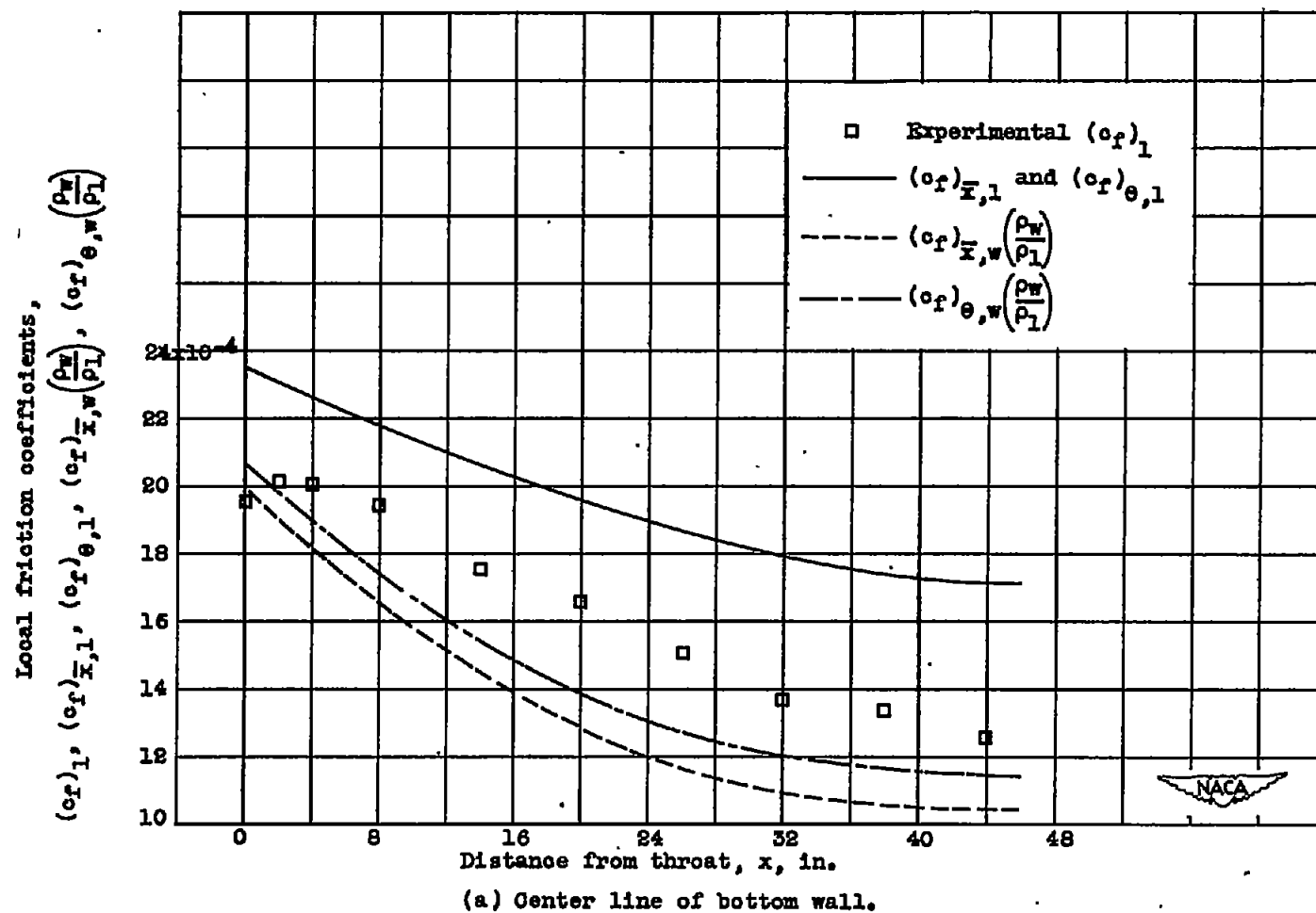
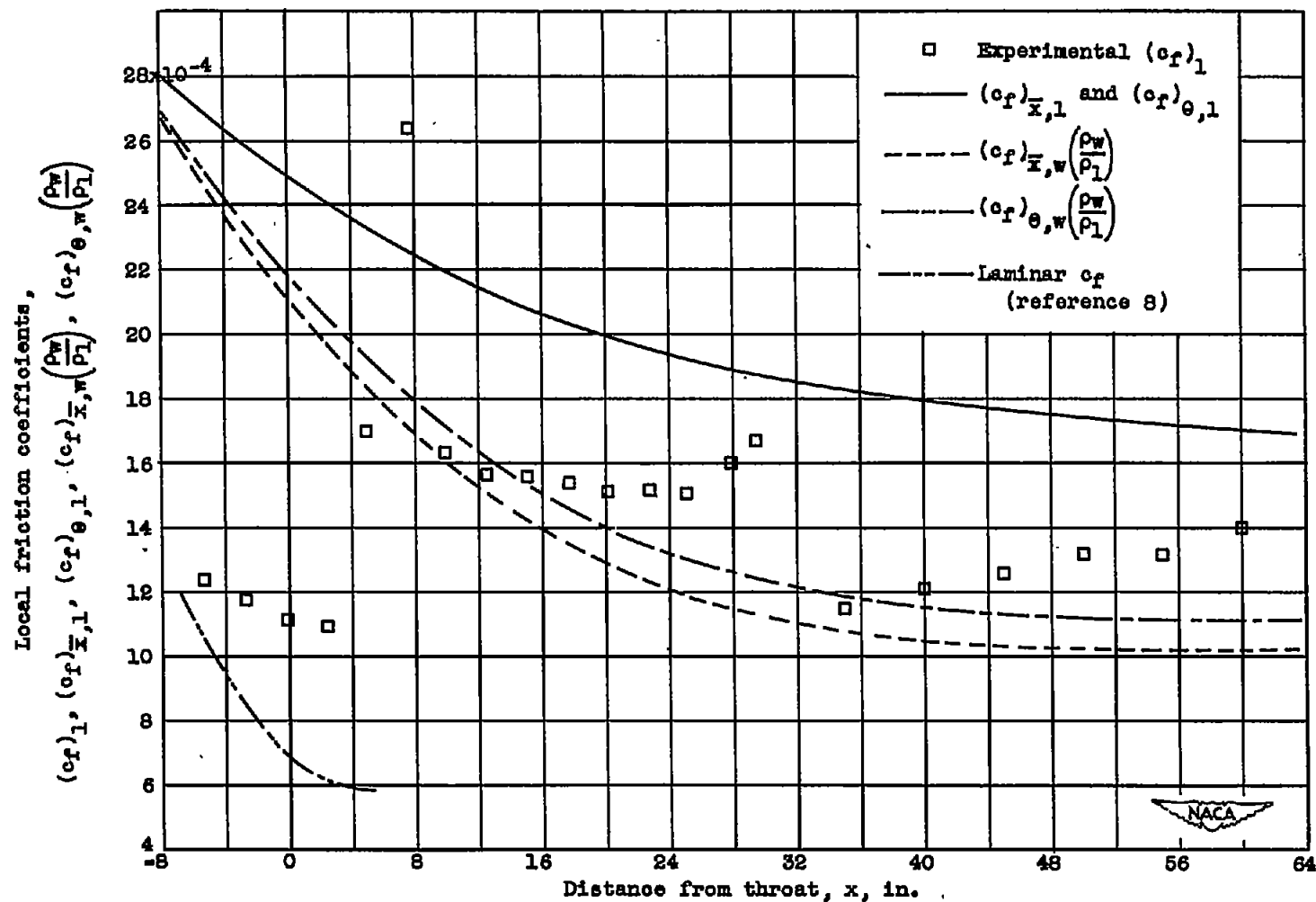


Figure 13. - Comparison of experimental and empirical skin-friction coefficients along channel at inlet pressure of 5 inches of mercury.



(b) Center line of side wall.

Figure 13. - Concluded. Comparison of experimental and empirical skin-friction coefficients along channel at inlet pressure of 5 inches of mercury.

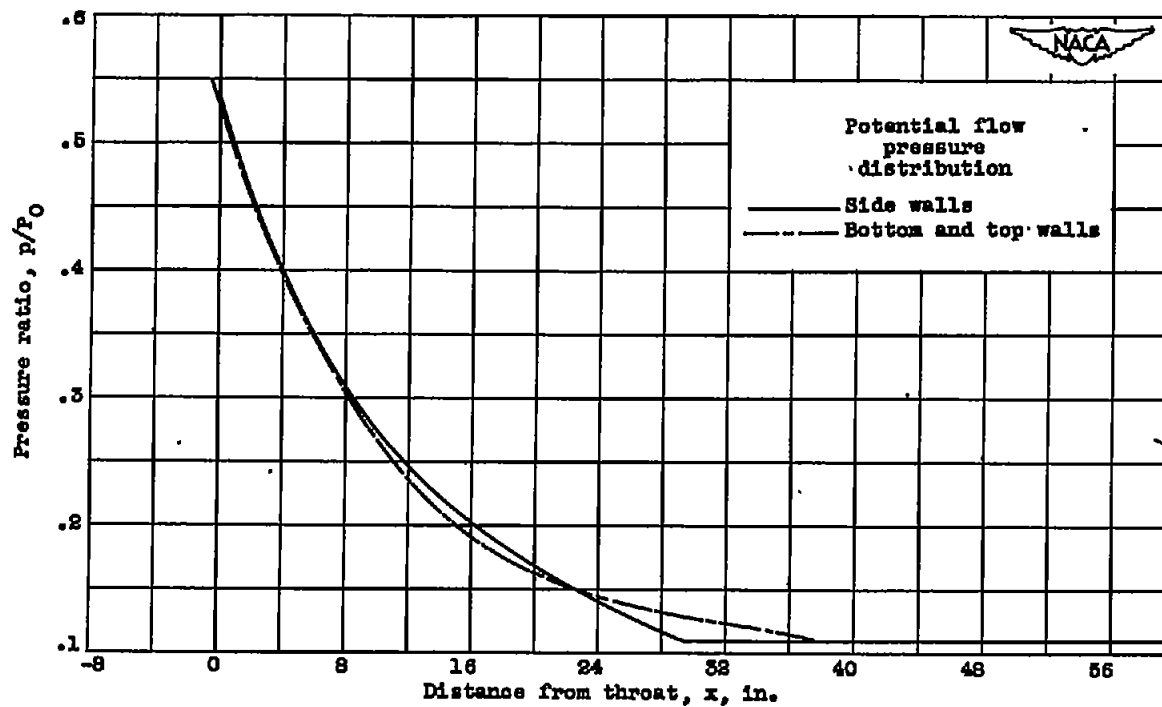
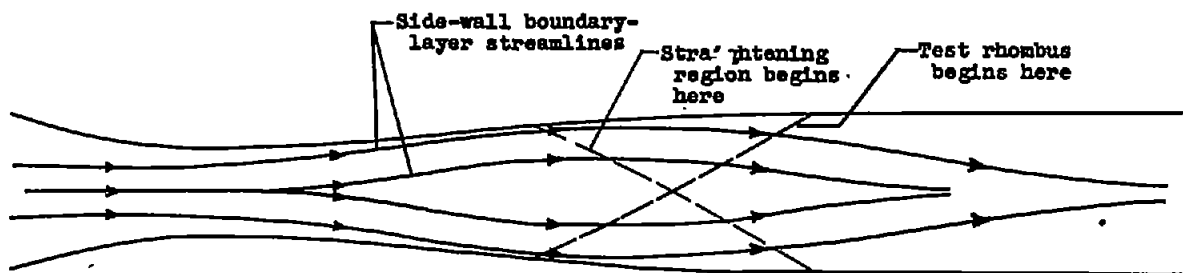


Figure 14. - Secondary flows in side-wall boundary layers.